

Modeling and Simulation of Transitional Taylor-Green Vortex Flow with PANS

F.S. Pereira^{1,*}, F.F. Grinstein¹, D.M. Israel¹, R. Rauenzahn¹, and S.S. Girimaji²

¹Los Alamos National Laboratory, X Division, Los Alamos, New Mexico, USA and

²Texas A&M University, Ocean Engineering, College Station, Texas, USA

A new PANS model is used to predict the transitional Taylor-Green vortex flow at initial Reynolds number 3000. This problem is a benchmark case for transitional flows in which the onset of turbulence is driven by vortex-stretching and reconnection mechanisms. Since these physical phenomena are observed in numerous flows of variable-density (e.g., oceanography and material mixing), this study constitutes the first step toward extending the PANS method to such a class of problems. We start by deriving the governing equations of the model and analyze the selection of the parameters controlling its physical resolution, f_ϵ and f_k , through *a-priori* testing. Afterward, we conduct PANS computations at different constant physical resolutions to evaluate the model's accuracy and cost predicting the TGV flow. This is performed through simple verification and validation exercises, and the physical and modeling interpretation of the numerical predictions. The results confirm that PANS can efficiently (accuracy vs. cost) predict the present flow problem. Yet, this is closely dependent on the physical resolution of the model. Whereas high-physical resolution ($f_k < 0.50$) computations are in good agreement with the reference DNS studies, low-physical resolution ($f_k \geq 0.50$) simulations lead to large discrepancies with the reference data. The physical and modeling interpretation of the results demonstrates that the origin of these distinct behaviors lies in the model's ability to capture the instabilities and coherent structures driving the onset of turbulence. The comparison of the computations' cost indicates that high-physical resolution PANS achieves the accuracy of DNS ($f_k = 0.00$) at a fraction of the cost. We observe a cost reduction of one order of magnitude at the current Re, which is expected to grow with Re. These results clearly indicate the potential of PANS to predict transitional flows efficiently.

I. INTRODUCTION

The onset of turbulence is a complex phenomenon governing the physics of numerous transient flows of practical interest - e.g., material mixing [1–3], combustion [4–6], astrophysics [7–9], and bluff-bodies in cross-flow [10–13]. Transition is characterized by its transient dynamics, sensitivity to the flow's geometry and initial conditions, triggering mechanisms [14–17], and dependence on hydrodynamic instabilities and coherent structures [18–28]. This set of features poses unique challenges to modeling and simulation of transitional flows.

Accurate computations of this class of problems are closely dependent on the mathematical model's ability to capture the fundamental physics of the onset, development, and decay of turbulence. Direct numerical simulation (DNS) and high-resolution large-eddy simulation (LES) [29–31] are the optimal techniques to predict transitional flows since these methods resolve all (DNS) or most (LES) flow scales. Yet, the caveat of such scale-resolving simulation (SRS) strategies is the inherent computational cost [32–34] and the difficulty of selecting proper initial and boundary flow conditions. The Reynolds-averaged Navier-Stokes (RANS) equations, on the other hand, reduce the cost burden of simulating transitional flows through its fully statistical description of turbulence, in which a closure models the entire spectrum of turbulence scales [35–38]. However, RANS closures have not been designed for transitional flows and, as such, often lead to inaccurate predictions [13, 35]. A

possible alternative to these modeling strategies is the utilization of bridging methods [39–43]. This class of SRS models can operate at any degree of physical resolution (from DNS to RANS) and has been expressly designed to efficiently (accuracy vs. cost) predict complex flows by resolving only the flow scales not amenable to modeling [12, 13]. The dynamics of the remaining scales can be accurately represented through an appropriate turbulence closure. In this manner, bridging models embed the concept of accuracy-on-demand, enabling significant enhancement of the efficiency of SRS predictions.

In recent years, the importance of predicting transitional flows has grown due to industrial needs and advances in computational capabilities. These provided the computational resources to allow scientists and engineers to study complex flows involving separation and transition. This has been driving intensive research in transition modeling and simulation, and diverse validation initiatives [44, 45] using benchmark problems. The Taylor-Green vortex (TGV) [46] is a test-case designed to study transition to turbulence driven by vortex-stretching and reconnection mechanisms [15, 47, 48]. This problem initially features multiple well-defined laminar vortices (figure 4), which interact and evolve in time. Their spatio-temporal development comprises five key stages:

- i) vortex stretching mechanisms generate vortex sheets which gradually get closer;
- ii) vortex sheets roll-up and reconnect [15, 48];
- iii) onset of turbulence and subsequent intensification of vorticity;
- iv) coherent structures breakdown and fully-developed turbulence;

* F.S. Pereira: fspereira@lanl.gov

v) turbulence decay.

There is a consensus that step *iii*) can involve multiple instabilities [24–28, 47]. In addition to the complex physics, this benchmark flow possesses well-characterized initial conditions which provide the consistency for rigorous verification and validation exercises. Brachet et al. [47] and Brachet [49] performed direct numerical simulations of the TGV flow at multiple Reynolds numbers to investigate the flow physics. These pioneering studies have been used as a reference in various numerical studies [48, 50–61].

This work investigates the ability of a bridging partially-averaged Navier-Stokes (PANS) equations method to predict the transitional TGV flow at Reynolds number 3000 [47]. Since our primary interest is variable-density flows and the present study constitutes the first step toward extending PANS to such class of flows, we use a simplified variable-density PANS closure based on Besnard-Harlow-Rauenzahn (BHR) multi-equation RANS framework [62] in the BHR-2 closure version [63]. The model's accuracy and cost is evaluated through simulation of the TGV flow at distinct constant degrees of physical resolution. This strategy prevents commutation errors [64] and enables robust verification and validation studies. The results are compared against the DNS data of Brachet et al. [47] and Drikakis et al. [51], and interpreted through the assessment of the coherent and turbulent flow fields.

The structure of this manuscript is as follows. Section II presents the derivation of the governing equations of PANS BHR-2. This step comprises the evaluation of the parameters defining the physical resolution of the model. Section III introduces the flow problem and the numerical settings of the computations. Section IV discusses the results of the study, and section V concludes the paper with the summary of the main findings.

II. GOVERNING EQUATIONS

The PANS equations are based upon the scale-invariance of the Navier-Stokes equations. This property has been initially demonstrated by Germano [65] for incompressible flow, and later extended to compressible flow by Suman and Girimaji [66]. To derive the governing equations of PANS, let us start by considering a general linear and constant preserving filtering operator, $\langle \cdot \rangle$. This filter commutes with spatial and temporal differentiation, and decomposes any instantaneous flow quantity, Φ , into a resolved/filtered, $\langle \Phi \rangle$, and unresolved/modeled, ϕ , component,

$$\Phi \equiv \langle \Phi \rangle + \phi . \quad (1)$$

From the concept of Favre-averaging [67–70], the former decomposition can be extended to variable-density (multi-material and/or compressible) flow,

$$\Phi \equiv \{ \Phi \} + \phi^* . \quad (2)$$

where $\{ \Phi \}$ and ϕ^* stand for the density-weighted resolved and unresolved fluctuating fraction of Φ . In the limit of all turbulent scales being modeled, relations 1 and 2 are equivalent to the Reynolds- [71] and Favre-averaged [67–70] decompositions,

$$\Phi \equiv \bar{\Phi} + \phi' , \quad (3)$$

$$\Phi \equiv \tilde{\Phi} + \phi'' , \quad (4)$$

where $\bar{\Phi}$ represents a Reynolds-averaged quantity, ϕ' the turbulent fluctuations, $\tilde{\Phi}$ a density-weighted quantity, and ϕ'' the fluctuations uncorrelated with the fluid's density ($\overline{\rho\phi''} = 0$).

The application of the filtering operators 1 and 2 to the Navier-Stokes equations for compressible flow leads to their filtered or partially-averaged form [65, 66],

$$\frac{\partial \langle \rho \rangle}{\partial t} + \frac{\partial (\langle \rho \rangle \{ V_i \})}{\partial x_i} = 0 , \quad (5)$$

$$\begin{aligned} \frac{\partial (\langle \rho \rangle \{ V_i \})}{\partial t} + \frac{\partial (\langle \rho \rangle \{ V_i \} \{ V_j \})}{\partial x_j} = & - \frac{\partial \langle P \rangle}{\partial x_i} + \frac{\partial \langle \sigma_{ij} \rangle}{\partial x_j} \\ & + \frac{\partial (\langle \rho \rangle \tau^1 (V_i, V_j))}{\partial x_j} , \end{aligned} \quad (6)$$

$$\begin{aligned} \frac{\partial (\langle \rho \rangle \{ E \})}{\partial t} + \frac{\partial (\langle \rho \rangle \{ E \} \{ V_j \})}{\partial x_j} = & - \frac{\partial (\langle \rho \rangle \tau^1 (V_j, E))}{\partial x_j} \\ & - \frac{\partial (\{ V_j \} \langle P \rangle)}{\partial x_j} - \frac{\partial \tau^2 (V_j, P)}{\partial x_j} \\ & + \frac{\partial (\{ V_i \} \langle \sigma_{ij} \rangle)}{\partial x_j} + \frac{\partial \tau^2 (V_i, \sigma_{ij})}{\partial x_j} , \\ & - \frac{\partial \langle q_j^c \rangle}{\partial x_j} \end{aligned} \quad (7)$$

where the unresolved turbulent stresses $\tau^1(\Phi_i, \Phi_j)$ and $\tau^2(\Phi_i, \Phi_j)$ are expressed in terms of generalized central second-moment tensors to guarantee scale-invariance [65]. These tensors account for the effect of the unresolved turbulent scales on the resolved field and are formally defined as [65, 66],

$$\tau^1(\Phi_i, \Phi_j) \equiv \{ \Phi_i, \Phi_j \} - \{ \Phi_i \} \{ \Phi_j \} , \quad (8)$$

$$\tau^2(\Phi_i, \Phi_j) \equiv \langle \Phi_i, \Phi_j \rangle - \{ \Phi_i \} \{ \Phi_j \} . \quad (9)$$

In equations 5 to 7, x_i are the coordinates of a Cartesian system, ρ is the fluid's density, V_i are the Cartesian velocity components, P is the pressure, σ_{ij} is the viscous-stress tensor assuming Newtonian fluid,

$$\langle \sigma_{ij} \rangle = 2\mu \{ S_{ij} \} - \frac{2}{3} \frac{\partial \{ V_k \}}{\partial x_k} \delta_{ij} \quad (10)$$

with $\{S_{ij}\}$ being the resolved strain-rate tensor,

$$\{S_{ij}\} = \frac{1}{2} \left(\frac{\partial\{V_i\}}{\partial x_j} + \frac{\partial\{V_j\}}{\partial x_i} \right), \quad (11)$$

μ is the dynamic viscosity, $E = \frac{1}{2}V_i^2 + e$ is the fluid's total energy, and e is the internal energy. The conductive heat flux q^c is neglected because the present TGV flow is characterized by negligible thermal effects. The pressure is calculated assuming a thermally perfect gas ($P = \rho RT$) so that its resolved component is written as follows [66],

$$\langle P \rangle = (\gamma - 1)\langle \rho \rangle \left(\{E\} - \frac{\{V_k\}\{V_k\}}{2} - k_u \right), \quad (12)$$

where T is the fluid's temperature, γ is the ratio between specific heats, and k_u is the unresolved or modeled turbulence kinetic energy. The generalized central second-moments create new variables that require modeling to close the system equations. This is accomplished through constitutive relationships.

II.1. Constitutive relationships

The generalized central second-moment tensor $\tau^1(V_i, V_j)$ represents the effect of the unresolved turbulence scales on the resolved velocity field. In BHR-2 closure [63], this tensor is modeled through the Boussinesq approximation [72], which establishes an analogy between the momentum transfer resultant from molecular gas and turbulent motion. Hence, $\tau^1(V_i, V_j)$ is assumed proportional to $\{S_{ij}\}$,

$$\tau^1(V_i, V_j) = 2\nu_u\{S_{ij}\} - \frac{2}{3}k_u\delta_{ij}. \quad (13)$$

In equation 13, ν_u is the turbulent kinematic viscosity of the unresolved or modeled scales. Throughout this work, the subscript u denotes the unresolved fraction of a given (PANS) turbulence quantity, whereas t indicates a total (RANS) turbulence variable. In the limit of all turbulence flow scales being modeled, the subscripts u and t are equivalent.

The remaining generalized central second-moment tensors invoke distinct constitutive relationships which derivation can be found in Besnard et al. [62], Suman and Girimaji [66], Zarlign et al. [63], and Schwarzkopf et al. [73]. In PANS form, these tensors lead to the following final form of the energy equation,

$$\begin{aligned} \frac{\partial(\langle \rho \rangle \{E\})}{\partial t} + \frac{\partial(\langle \rho \rangle \{E\} \{V_j\})}{\partial x_j} &= - \frac{\partial(\{V_j\} \langle P \rangle)}{\partial x_j} \\ &+ \frac{\partial(\{V_j\} \langle \sigma_{ij} \rangle)}{\partial x_j} + \frac{\partial(\langle \rho \rangle \{V_j\} \tau^1(V_i, V_j))}{\partial x_j}, \\ &+ \frac{\partial}{\partial x_j} \left[\left(\mu + \frac{\mu_u}{\sigma_k} \right) \frac{\partial k_u}{\partial x_j} \right] \end{aligned} \quad (14)$$

where σ_k is a coefficient. The former relations introduce two additional variables, k_u and ν_u , which need modeling to close the governing equations of PANS.

II.2. PANS BHR-2 closure

In this work, the dynamics of the unresolved turbulent scales is represented through a variable-density PANS closure based on Besnard-Harlow-Rauenzahn (BHR) multi-equation RANS model [62] in the BHR-2 closure version [63]. Such RANS closure is featured by six dependent variables: turbulence kinetic energy, k_t , turbulence dissipation length-scale, S_t , velocity mass flux, a_{i_t} , and density-specific volume correlation, b_t . Since the last two quantities, a_{i_t} and b_t , are not relevant for the present TGV computations, their equations will be presented in future work.

The BHR-2 RANS closure calculates the total kinematic turbulent viscosity, ν_t , as

$$\nu_t = \frac{\mu_t}{\rho} = c_\mu S_t \sqrt{k_t}, \quad (15)$$

where c_μ is a coefficient given in table I, S_t is the turbulence dissipation length-scale,

$$S_t = \frac{k_t^{3/2}}{\varepsilon_t}, \quad (16)$$

and ε_t is the dissipation of k_t . BHR-2 models the former turbulence quantities, k_t and S_t , through the following evolution equations,

$$\frac{\partial k_t}{\partial t} + \tilde{V}_j \frac{\partial k_t}{\partial x_j} = \mathcal{P}_{b_t} + \mathcal{P}_{s_t} - \frac{k_t^{3/2}}{S_t} + \frac{1}{\rho} \frac{\partial}{\partial x_j} \left(\frac{\rho \nu_t}{\sigma_k} \frac{\partial k_t}{\partial x_j} \right), \quad (17)$$

$$\begin{aligned} \frac{\partial S_t}{\partial t} + \tilde{V}_j \frac{\partial S_t}{\partial x_j} &= \frac{S_t}{k_t} (c_4 \mathcal{P}_{b_t} + c_1 \mathcal{P}_{s_t}) - c_2 \sqrt{k_t} \\ &+ \frac{1}{\rho} \frac{\partial}{\partial x_j} \left(\frac{\rho \nu_t}{\sigma_S} \frac{\partial S_t}{\partial x_j} \right) \end{aligned} \quad (18)$$

where \mathcal{P}_{b_t} and \mathcal{P}_{s_t} are the total production of turbulence kinetic energy by buoyancy and shear effects. The first production mechanism of k_t is modeled as,

$$\mathcal{P}_{s_t} = -R(V_i, V_j) \frac{\partial \tilde{V}_i}{\partial x_j}, \quad (19)$$

whereas the second is neglected in this work owing to the fact that the TGV is a single-fluid and (nearly) incompressible flow problem. In equation 19, $R(V_i, V_j)$ stands for the specific total turbulent or Reynolds-stress tensor - $R(V_i, V_j) = \tau(V_i, V_j)$ for $f_k = f_\varepsilon = 1.00$. The coefficients c_μ , c_1 , c_2 , σ_k , σ_S are given in table I [63].

The former set of governing equations has been developed to operate with RANS variables: $\tilde{\Phi}$, $\bar{\Phi}$, or Φ_t . We now derive their PANS counterpart [41]. Toward this end, the parameters defining the ratios of modeled-to-total turbulence kinetic energy and dissipation length-scale,

$$f_k \equiv \frac{k_u}{k_t}, \quad f_S \equiv \frac{S_u}{S_t}, \quad (20)$$

need to be included in equations 17 and 18. These enable the BHR-2 closure to operate at any degree of physical resolution, i.e., from RANS to DNS. The ratio of modeled-to-total turbulence dissipation length-scale, f_S , can also be defined as follows,

$$f_S \equiv \frac{S_u}{S_t} = \left(\frac{k_u^{3/2}}{\varepsilon_u} \right) \left(\frac{\varepsilon_t}{k_t^{3/2}} \right) = \frac{f_k^{3/2}}{f_\varepsilon}, \quad (21)$$

where f_ε is the ratio of modeled-to-total turbulence dissipation. Since f_ε is physically more intuitive than f_S , the evolution equations for k_u and S_u are derived in terms of f_k and f_ε .

II.2.1. k_u evolution equation

It has been demonstrated by Girimaji [41] and Suman and Girimaji [66] that the scale-invariant form of the evolution equation for k_u can be written as follows,

$$\frac{\partial k_u}{\partial t} + \{V_j\} \frac{\partial k_u}{\partial x_j} = \mathcal{P}_{s_u} - \mathcal{E}_u + \mathcal{T}_u, \quad (22)$$

where \mathcal{P}_{s_u} , \mathcal{E}_u and \mathcal{T}_u represent the production by shear mechanisms, dissipation, and transport of unresolved turbulence kinetic energy, k_u . For constant f_k , differentiation commutes in time and space and so it is possible to establish a relationship between the evolution equation for total (RANS) and partial (PANS) turbulence kinetic energy,

$$\frac{\partial k_u}{\partial t} + \tilde{V}_j \frac{\partial k_u}{\partial x_j} = f_k \left[\frac{\partial k_t}{\partial t} + \tilde{V}_j \frac{\partial k_t}{\partial x_j} \right]. \quad (23)$$

Considering that PANS calculates filtered or partial dependent variables, the left-hand side of the former equation can be rewritten as,

$$\frac{\partial k_u}{\partial t} + \{V_j\} \frac{\partial k_u}{\partial x_j} = f_k \left[\frac{\partial k_t}{\partial t} + \tilde{V}_j \frac{\partial k_t}{\partial x_j} \right] + (\{V_j\} - \tilde{V}_j) \frac{\partial k_u}{\partial x_j}. \quad (24)$$

Replacing the first term of the right-hand side by that of equation 17 ($\mathcal{P}_{b,t} = 0$),

$$\begin{aligned} \frac{\partial k_u}{\partial t} + \{V_j\} \frac{\partial k_u}{\partial x_j} &= f_k \left[\mathcal{P}_{s_t} - \frac{k_t^{3/2}}{S_t} + \frac{1}{\bar{\rho}} \frac{\partial}{\partial x_j} \left(\frac{\mu_t}{\sigma_k} \frac{\partial k_t}{\partial x_j} \right) \right], \\ &+ (\{V_j\} - \tilde{V}_j) \frac{\partial k_u}{\partial x_j} \end{aligned} \quad (25)$$

TABLE I: Coefficients of BHR-2 closure.

c_1	c_2	c_μ	σ_k	σ_S
0.06	-0.42	0.28	1.00	0.10

and applying a similar procedure to the left-hand side, the following relation is obtained,

$$\begin{aligned} \mathcal{P}_{s_u} - \mathcal{E}_u + \mathcal{T}_u &= f_k \left[\mathcal{P}_{s_t} - \frac{k_t^{3/2}}{S_t} + \frac{1}{\bar{\rho}} \frac{\partial}{\partial x_j} \left(\frac{\bar{\rho} \nu_t}{\sigma_k} \frac{\partial k_t}{\partial x_j} \right) \right] \\ &+ (\{V_j\} - \tilde{V}_j) \frac{\partial k_u}{\partial x_j} \end{aligned} \quad (26)$$

This equation illustrates the formal similarity between PANS (left-hand side) and RANS (right-hand side) production, dissipation, and transport terms. It is therefore possible to relate the source and sink terms of equation 26,

$$\mathcal{P}_{s_u} - \frac{k_u^{3/2}}{S_u} = f_k \left[\mathcal{P}_{s_t} - \frac{k_t^{3/2}}{S_t} \right] = f_k \left[\mathcal{P}_{s_t} - \frac{1}{f_\varepsilon} \frac{k_u^{3/2}}{S_u} \right], \quad (27)$$

to obtain an expression for \mathcal{P}_{s_t} in terms of unresolved quantities, f_k , and f_ε ,

$$\mathcal{P}_{s_t} = \frac{1}{f_\varepsilon} \left(\frac{k_u^{3/2}}{S_u} \right) + \frac{1}{f_k} \left(\mathcal{P}_{s_u} - \frac{k_u^{3/2}}{S_u} \right). \quad (28)$$

This relation is used in the derivation of the evolution equation for S_u . On the other hand, the transport terms \mathcal{T}_u and \mathcal{T}_t can be related as follows,

$$\begin{aligned} \mathcal{T}_u &= f_k \left[\frac{1}{\bar{\rho}} \frac{\partial}{\partial x_j} \left(\frac{\bar{\rho} \nu_t}{\sigma_k} \frac{\partial k_t}{\partial x_j} \right) \right] + (\{V_j\} - \tilde{V}_j) \frac{\partial k_u}{\partial x_j} \\ &= \frac{1}{\langle \rho \rangle} \frac{\partial}{\partial x_j} \left(\frac{\langle \rho \rangle \nu_u}{\sigma_k} \frac{f_\varepsilon}{f_k^2} \frac{\partial k_u}{\partial x_j} \right) + (\{V_j\} - \tilde{V}_j) \frac{\partial k_u}{\partial x_j} \end{aligned} \quad (29)$$

Using scaling arguments, Girimaji [41] showed that

$$(\{V_j\} - \tilde{V}_j) \frac{\partial k_u}{\partial x_j} \approx 0, \quad (30)$$

leading to the so-called zero-transport model (ZTM). The accuracy of this model has been confirmed in the recent work of Tazraei and Girimaji [74]. Also, it is important to highlight that the velocity difference term tends to zero in the limit of $f_k = 0.00$ and 1.00 since

$$\{V_j\} - \tilde{V}_j = 0 \text{ at } f_k = 0.0, \quad \frac{\partial k_u}{\partial x_j} = 0 \text{ at } f_k = 1.0. \quad (31)$$

This further reaffirms the validity of the ZTM. The derivation of the evolution equation for k_u concludes by combining equations 25, 29 and 30, this leading to its final form,

$$\frac{\partial k_u}{\partial t} + \{V_j\} \frac{\partial k_u}{\partial x_j} = \mathcal{P}_{s_u} - \frac{k_u^{3/2}}{S_u} + \frac{1}{\langle \rho \rangle} \frac{\partial}{\partial x_j} \left(\frac{\langle \rho \rangle \nu_u}{\sigma_k} \frac{f_\varepsilon}{f_k^2} \frac{\partial k_u}{\partial x_j} \right), \quad (32)$$

where

$$\mathcal{P}_{s_u} = -\tau(V_i, V_j) \frac{\partial \{V_i\}}{\partial x_j}. \quad (33)$$

We recall that the derivation of equation 32 relies on the assumption that the filtering operator commutes with spatial and temporal differentiation. If this property does not hold, the model's derivation needs to consider additional terms [75] and the modeled-to-total ratio of density, f_ρ . Despite being commonly neglected, this requirement holds for any bridging or hybrid formulation.

II.2.2. S_u evolution equation

Similarly to k_u , the derivation of the evolution equation for S_u starts by establishing a relationship between the equations for S_t (RANS) and S_u (PANS),

$$\frac{\partial S_u}{\partial t} + \tilde{V}_j \frac{\partial S_u}{\partial x_j} = f_S \left[\frac{\partial S_t}{\partial t} + \tilde{V}_j \frac{\partial S_t}{\partial x_j} \right]. \quad (34)$$

This equation can be rewritten as,

$$\frac{\partial S_u}{\partial t} + \{V_j\} \frac{\partial S_u}{\partial x_j} = f_S \left[\frac{\partial S_t}{\partial t} + \tilde{V}_j \frac{\partial S_t}{\partial x_j} \right] + (\{V_j\} - \tilde{V}_j) \frac{\partial S_u}{\partial x_j}, \quad (35)$$

so that the left-hand side contains only PANS variables. Then, applying the zero transport model [41] and replacing the material derivative of S_t by the right-hand side of equation 18 ($\mathcal{P}_{b,t} = 0$) leads to,

$$\begin{aligned} \frac{\partial S_u}{\partial t} + \{V_j\} \frac{\partial S_u}{\partial x_j} = f_S & \left[\frac{S_t}{k_t} c_1 \mathcal{P}_{s_t} - c_2 \sqrt{k_t} \right] \\ & + f_S \left[\frac{1}{\bar{\rho}} \frac{\partial}{\partial x_j} \left(\frac{\bar{\rho} \nu_t}{\sigma_S} \frac{\partial S_t}{\partial x_j} \right) \right]. \end{aligned} \quad (36)$$

Finally, using equations 20, 21 and 28, the evolution equation for S_u reads as,

$$\begin{aligned} \frac{\partial S_u}{\partial t} + \{V_j\} \frac{\partial S_u}{\partial x_j} = c_1 \frac{S_u}{k_u} \mathcal{P}_{s_u} - c_2^* \sqrt{k_u} \\ + \frac{1}{\langle \rho \rangle} \frac{\partial}{\partial x_j} \left(\frac{\langle \rho \rangle \nu_u}{\sigma_S} \frac{f_\varepsilon}{f_k^2} \frac{\partial S_u}{\partial x_j} \right), \end{aligned} \quad (37)$$

where

$$c_2^* = c_1 \left(1 - \frac{f_k}{f_\varepsilon} \right) + c_2 \frac{f_k}{f_\varepsilon}. \quad (38)$$

II.3. Filter control parameter

The success of bridging methods is closely dependent on the physical resolution, i.e., the range of resolved flow scales. In PANS, this property is controlled by f_ϕ parameters (relations 20 and 21). As the physical resolution increases, a wider range of flow scales is resolved and the numerical resolution necessary to accurately capture these physically resolved scales grows. Whereas excessively large physical resolutions lead to inefficient (accuracy vs. cost) calculations, reduced values of this parameter may reveal insufficient to resolve the flow phenomena

not amenable to modeling [12, 13, 76, 77]. Since in practical problems the numerical resources are fixed, the selection of the physical resolution determines the efficiency and, consequently, the success of bridging computations.

The efficient determination of the physical resolution for given bridging model, flow problem, and quantities of interest considers three main factors:

- i) the length and time scales of the flow structures that need to be resolved;
- ii) the smallest flow scales that a given spatio-temporal grid resolution (and numerical scheme) can accurately predict;
- iii) the impact of the physical resolution on the closure's turbulence dependent quantities.

The first aspect has been recently addressed by Pereira et al. [12, 13, 76, 78] for flows past circular cylinders in the sub-critical regime. Supported by experimental evidence, these studies show that the simulations' accuracy is determined by the ability of the turbulence model (RANS or SRS) to predict the spatial development of the coherent structures governing the flow dynamics: the vortex-shedding and Kelvin-Helmholtz structures. The latter phenomenon is responsible for driving the dynamics of the onset of turbulence in the free shear-layers of the cylinder, this being featured by smaller wavelengths/frequencies than the vortex-shedding. Hence, and since they are not amenable to modeling by one-point closures, the Kelvin-Helmholtz instability and rollers determine the physical resolution needed for such class of flow problems.

The second point is ideally addressed through verification exercises [79–81]. Nevertheless, it is possible to obtain a loose *a-priori* estimate of the maximum physical resolution that a spatio-temporal grid resolution can support, as well as the effect of increasing the physical resolution on the numerical requirements of the simulations. At a minimum, the largest grid cell size, Δ , needs to have the size of the smallest resolved flow scales, η_r ,

$$\Delta \leq \eta_r. \quad (39)$$

Adapting the Kolmogorov arguments to resolved fluid motions,

$$\Delta \sim \left(\frac{\nu_u^3}{\varepsilon_t} \right)^{0.25}, \quad (40)$$

assuming high-Re flow ($f_\varepsilon = 1.0$), and using equation 15 for the unresolved field, the following expression for Δ is obtained,

$$\Delta \approx C_\mu^{0.75} \frac{k_t^{1.5}}{\varepsilon_t} f_k^{1.5}. \quad (41)$$

This relation can be rewritten to provide an estimate for the smallest f_k that a given spatial grid resolution can support,

$$f_k \geq \left(\frac{1}{C_\mu} \right)^{0.5} \left(\frac{\Delta}{k_t^{1.5}/\varepsilon_t} \right)^{2/3}, \quad (42)$$

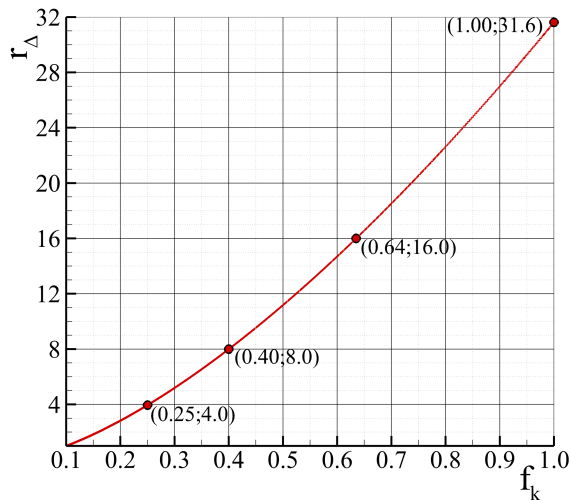


FIG. 1: Ratio between the minimum spatial grid resolution needed for computations at a given f_k and $(f_k)_{\text{ref}} = 0.10$, r_Δ .

or to estimate the ratio between the smallest grid size for two values of f_k ,

$$r_\Delta = \frac{\Delta_{f_k}}{\Delta_{(f_k)_{\text{ref}}}} = \left[\frac{f_k}{(f_k)_{\text{ref}}} \right]^{1.5}, \quad (43)$$

where the subscript “ref” denotes a reference f_k . This last expression enables the assessment of the relative evolution of Δ with f_k , and it is depicted in figure 1 for $(f_k)_{\text{ref}} = 0.10$. As expected, $r_\Delta(f_k)$ indicates that the spatial grid resolution increases with the physical resolution ($f_k \rightarrow 0$). For instance, figure 1 shows that the necessary grid resolution for simulations conducted at $f_k = 0.25$ and 0.40 is approximately 4 and 8 times coarser than at $f_k = 0.10$, $r_\Delta = 4$ and 8 . Considering that SRS computations are inherently three dimensional and time-dependent, this simple analysis illustrates the potential of bridging formulations to reduce the cost of SRS calculations. Also, it emphasizes the importance of selecting adequate physical resolution for a given problem and quantities of interest.

The third aspect stems from the fact that the physical resolution often affects the turbulence dependent quantities differently, i.e., a given range of resolved scales is not expected to lead to equal ratios of modeled-to-total of all turbulence dependent quantities. Considering the case of BHR-2 closure, it is well-known that the spectral properties of k and ε are distinct [37] so that f_k and f_ε should only be equal in the limit of all scales being modeled or resolved. Although most SRS formulations neglect this crucial feature, PANS can account for its effects by considering the ratio modeled-to-total ratio, f_ϕ , of each turbulent dependent quantity. However, the magnitude of these parameters needs to be determined.

As previously mentioned, the current version of PANS BHR-2 relies on f_k and f_ε to set the model’s physical resolution. The parameter f_k can be either defined constant [41, 78, 82, 83] or dynamically [82, 84–86] in space and

time. Whereas the first approach prevents commutation errors and the entanglement of numerical and modeling errors, the second can enhance the computations’ efficiency. In this work, we choose to conduct all PANS simulations at constant f_k to avoid commutation errors and perform robust verification and validation exercises. On the other hand, f_ε is usually defined as constant and equal to one. This option has been motivated by the fact that most turbulence dissipation at high-Re flows is expected to occur at the smallest and dissipative scales [37, 87]. Thus, $f_\varepsilon = 1.00$ is generally accepted as a reasonable assumption for bridging models operating between RANS and LES. Yet, this assumption has not been verified.

To confirm its validity for practical turbulent flows, we perform *a-priori* testing to calculate f_k and f_ε at successively smaller physical resolutions - ranging from DNS ($f_k = 0.00$) to RANS ($f_k = 1.00$). The selected problem is the forced homogeneous turbulent flow at Taylor Reynolds numbers $\text{Re}_\lambda = 140$ and 300 predicted by Silva et al. [88] utilizing direct numerical simulations. k_u and ε_u are computed as follows. The velocity field of the data sets of Silva et al. [88] is first filtered by applying the following spatial filtering operator [89, 90],

$$\langle \Phi \rangle(\mathbf{x}) = \int_{-\Delta/2}^{+\Delta/2} \int_{-\Delta/2}^{+\Delta/2} \int_{-\Delta/2}^{+\Delta/2} \Phi(\mathbf{x}) G_\Delta(\mathbf{x} - \mathbf{x}') d\mathbf{x}', \quad (44)$$

where bold symbols denote vectors, and Δ and G_Δ are the filter’s width and kernel, respectively. In this exercise, we use a box filter so that

$$G_\Delta(\mathbf{x} - \mathbf{x}') = \begin{cases} \Delta^{-3} & , |\mathbf{x} - \mathbf{x}'| < 0.5\Delta \\ 0 & , \text{otherwise} \end{cases}. \quad (45)$$

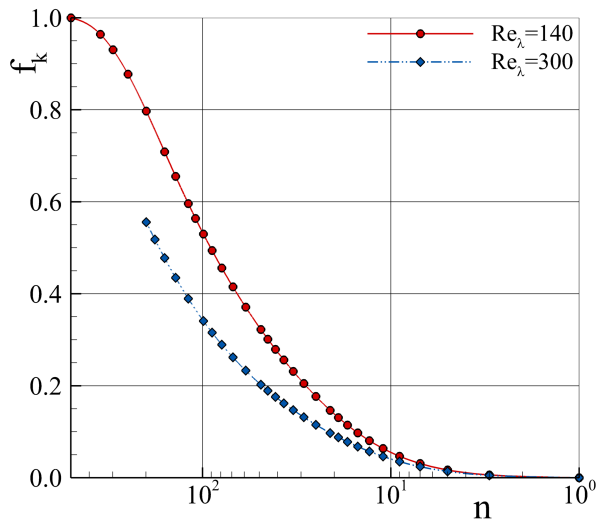
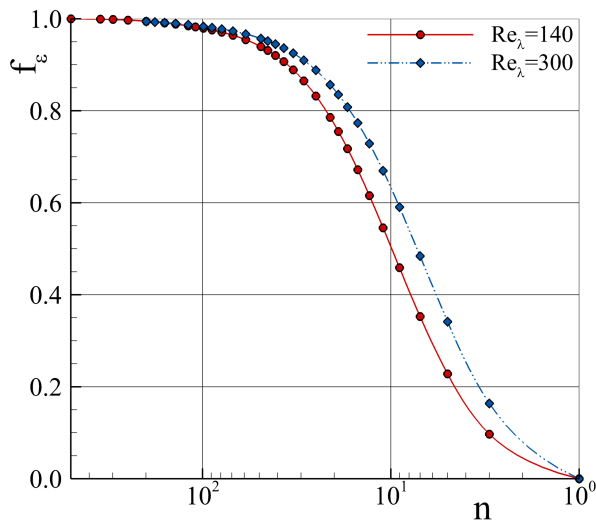
As discussed in da Silva and Pereira [91], Borue and Orzag [92], and Liu et al. [93], the utilization of box and Gaussian filters is not expected to influence the results of this class of studies. In contrast, cut-off filters are not suitable for this exercise since practical SRS computations do not rely on such operators [91, 94]. It is also generally accepted that the box filtering operator is the closest approach to the implicit filtering of finite-difference or -volume discretization schemes utilized in engineering computations [90, 95, 96]. Once the velocity field is filtered, k_u and ε_u are computed from relation 8 [65],

$$k_u = 0.5 \sum_{i=1}^3 (\langle V_i V_i \rangle - \langle V_i \rangle \langle V_i \rangle), \quad (46)$$

$$\varepsilon_u = \nu \sum_{i=1}^3 \left(\left\langle \frac{\partial V_i}{\partial x_i} \frac{\partial V_i}{\partial x_i} \right\rangle - \left\langle \frac{\partial V_i}{\partial x_i} \right\rangle \left\langle \frac{\partial V_i}{\partial x_i} \right\rangle \right). \quad (47)$$

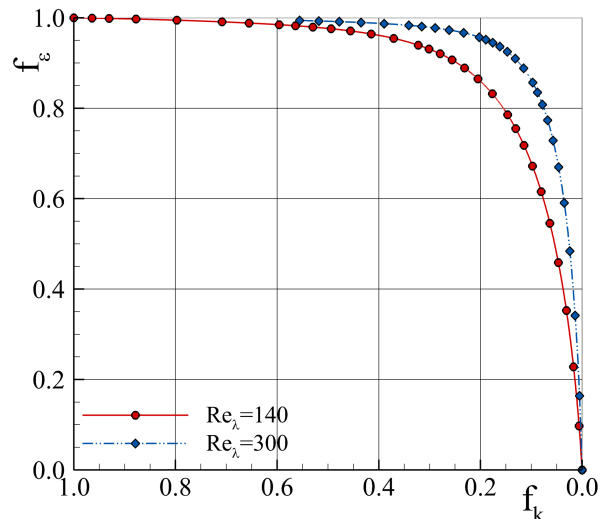
These quantities have been calculated with $n = \Delta/\Delta x$ up to 349, with Δx the grid size of the DNS simulations.

The variation of f_k and f_ε with n is depicted in figure 2. Referring to $f_k(n)$, the results indicate that most

(a) $f_k(n)$.(b) $f_\varepsilon(n)$.FIG. 2: Evolution of f_k and f_ε with the relative filter size, n , at $\text{Re}_\lambda = 140$ and 300.

turbulence kinetic energy is at the largest scales. Also, this tendency becomes more pronounced with Re_λ . For instance, the data shows that $\text{Re}_\lambda = 140$ and 300 require $n = 29$ and 49 to filter 20% of k_t ($f_k = 0.20$). This outcome highlights the potential of bridging models to reduce the computing cost of simulations of turbulence. It is also interesting to observe that from $f_k = 0.00$ to 0.20, the grid resolution/filter size grows more than one order of magnitude. In contrast, figure 2b shows that most turbulence dissipation occurs at the smallest scales and, as such, f_ε grows more rapidly with n than f_k . The data indicates that $f_\varepsilon = 0.22$ ($\text{Re}_\lambda = 140$) and 0.34 ($\text{Re}_\lambda = 300$) for $n = 5$. For $n = 199$, this parameter exceeds 0.99 for both Re_λ .

Next, figure 3 plots f_ε as a function of f_k for both Reynolds numbers. It is observed that once $f_k = 0.20$, $f_\varepsilon = 0.87$ for $\text{Re}_\lambda = 140$, and $f_\varepsilon = 0.93$ for $\text{Re}_\lambda = 300$.

FIG. 3: Evolution of f_k with f_ε at $\text{Re}_\lambda = 140$ and 300.

In this manner, and considering that practical SRS are not intended to operate at $f_k < 0.20$ due to the associated cost, the data confirm that assuming $f_\varepsilon = 1.00$ is a reasonable assumption for practical PANS calculations.

Notwithstanding these results, it is important to mention that f_k and f_ε might be affected by the dynamics of transient flow problems, reducing the differences between these parameters at high physical resolutions. In these cases, the exact selection of such parameters would ideally require a dynamic approach. Yet, and in addition to commutation errors, the development of such strategy is complex for transient flows owing to their dependence on the flow properties, time-instant, and zone. For these reasons, we prefer using constant values of f_k and $f_\varepsilon = 1.00$ even if at the possible expense of further reducing f_k to compensate calibration deficits at early flow instants.

III. PROBLEM SETUP

The TGV [46] is a paradigmatic test-case used to study modeling and simulation of onset, development and decay of turbulence. This problem is initially characterized by several laminar, well-characterized, and single-mode vortices, figure 4. These structures evolve and interact in time, this leading to five major flow stages: *i*) vortex stretching mechanisms generate vortex sheets which gradually get closer; *ii*) vortex sheets roll-up and reconnect [15, 48]; *iii*) onset of turbulence and subsequent intensification of vorticity; *iv*) coherent structures breakdown and fully developed turbulence; and *v*) turbulence decay.

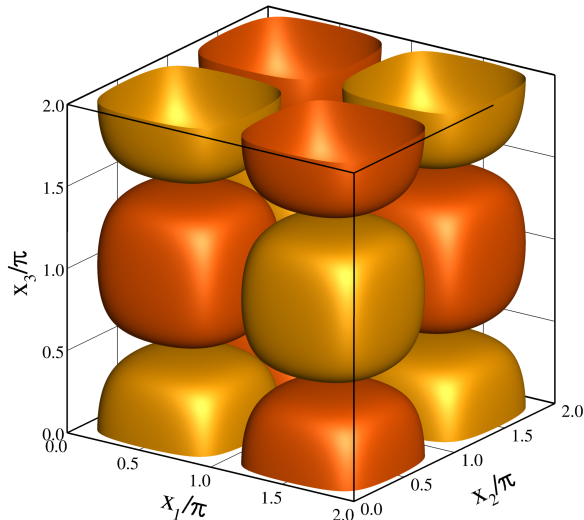
The initial velocity field of the TGV problem is given by [46, 47],

$$V_1(\mathbf{x}, t_o) = V_o \sin(x_1) \cos(x_2) \cos(x_3) , \quad (48)$$

$$V_2(\mathbf{x}, t_o) = -V_o \cos(x_1) \sin(x_2) \cos(x_3) , \quad (49)$$

TABLE II: Initial flow and thermodynamic fluid properties.

Ma_o	V_o (cm/s)	L_o (cm)	ρ_o (g/cm ³)	P_o (Pa)	μ (g/(cm.s))	γ	k_o (cm ² /s ²)	S_o (cm)
0.28	10^4	1.00	1.178×10^{-3}	10^5	3.927×10^{-3}	0.40	10^{-7}	6.136×10^{-3}

FIG. 4: Iso-surfaces of the vorticity x_3 -component at $t = 0$.

$$V_3(\mathbf{x}, t_o) = 0, \quad (50)$$

where V_o is the initial velocity magnitude. Figure 4 illustrates the initial flow field. The pressure is obtained from solving the Poisson equation,

$$P(\mathbf{x}, t_o) = P_o + \frac{\rho_o V_o^2}{16} [2 + \cos(2x_3)] [\cos(2x_1) + \cos(2x_2)], \quad (51)$$

where P_o and ρ_o stand for the pressure and density at the initial time instant, $t = 0$. The calculations are conducted with the compressible xRage solver [97] using an ideal gas equation of state and setting the initial Mach number, Ma_o , equal to 0.28. This leads to maximum instantaneous and averaged (L_1 norm) variations of ρ smaller than 11.0% and 1.4% of ρ_o for $f_k = 0.00$, respectively. The Reynolds number, $Re = \rho L_o V_o / \mu$, is set equal to 3000 to replicate the simulations of Brachet et al. [47]. The initial flow and thermodynamic fluid properties are summarized in table II.

xRage utilizes a finite volume approach to solve the compressible and multi-material conservation equations for mass, momentum, energy, and species concentrations. The resulting system of governing equations is resolved through the HLLC [98] Riemann solver using a directionally unsplit strategy, direct remap, parabolic reconstruction [99], and the low Mach number correction proposed by Thornber et al. [100]. The equations are discretized with second-order accurate methods: the temporal discretization relies on the explicit Runge-Kutta scheme known as Heun's method, whereas the spatial discretization is based on a Godunov scheme. The time-

step is defined by imposing a maximum CFL number,

$$\Delta t = \frac{\Delta x \cdot \text{CFL}}{N(|V| + c)}, \quad (52)$$

equal to 0.45, where c is the speed of sound, and N is the number of spatial dimensions. The modeling of high convection-driven flows is performed with a van-Leer limiter [101], without artificial viscosity. The thermal flux, q^c , of the PANS equations is neglected due to its negligible importance to the selected problem.

In order to mimic the original problem setup [46], the computational domain is a cube of width equal to 2π cm (figure 4). The computations are conducted using four grid resolutions, $N_c = 128^3, 256^3, 512^3$, and 1024^3 cells. PANS simulations are performed at six different and constant values of f_k : 0.00 (no closure), 0.25, 0.35, 0.50, 0.75 and 1.00 (RANS). This strategy enables us to evaluate the dependence of PANS on the range of resolved scales, enable rigorous verification and validation errors, and prevent commutation errors [64]. f_ε , on the other hand, is set equal to one (see section II.3). The initial conditions of PANS BHR-2 dependent variables are set as $k = k_o f_k$ and $S = S_o f_k^{1.5} / f_\varepsilon$, where k_o and S_o are given in table II. The simulations are compared against those of Brachet et al. [47] and Drikakis et al. [51]. It is important to note that these reference studies do not report estimates of numerical uncertainty, and Brachet et al. [47] seem to use a computational domain with a length of πL_o instead of $2\pi L_o$ and an incompressible flow solver.

IV. RESULTS AND DISCUSSION

We initiate the discussion of the results in Section IV.1 with a succinct description of the temporal evolution of the TGV flow. This constitutes a crucial step to understand the physics of the numerical results. Afterward, Section IV.2 discusses the effect of the physical resolution on the numerical and modeling accuracy of PANS calculations. This is accomplished through simple verification and validation exercises using the DNS data of Brachet et al. [47] and Drikakis et al. [51]. The discussion of the results also includes their physical interpretation in Section IV.3, and concludes with the comparison of the simulations' cost in Section IV.4. All results are normalized by ρ_o, V_o , and L_o .

IV.1. Temporal flow evolution

The TGV is a transient flow problem which includes laminar flow, instabilities and coherent structures, onset

and development of turbulence, and rapid kinetic energy decay due to turbulent viscous effects. To understand the multiple stages of the TGV flow, figure 5 depicts the temporal evolution of the coherent field using the λ_2 -criterion proposed by Jeong and Hussain [102]. The present analysis was repeated with the vorticity magnitude and Q -[103] criteria to assess its dependence on the method used to identify the vortical structures of the flow [102]. The results revealed that the three criteria tested do not alter the conclusions of the present analysis. For the sake of clearness and considering the symmetries of the TGV problem, figure 5 only depicts half of the computational domain, $0 \leq x_3 \leq \pi$.

Figure 5 shows that the TGV flow is initially characterized by the set of laminar, well-defined, and symmetric vortices given by equations (48-50). After this initial time instant, $t = 0$, the vortical structures interact and develop, this leading the loss of symmetry and deformation observed in figure 5b ($t = 1.0$). In the following instants ($2 \leq t \leq 4$), the vortices continue evolving, and vortex-stretching processes lead to the generation of pairs of long sheet-like structures. These pairs of counter-rotating vortical structures get closer, and the resulting interactions lead to their rapid deformation ($t = 4.0$). From $t = 5$ to 6, it is possible to visualize a complex reconnection [15, 47] mechanism between pairs of counter-rotating vortices. Also, there is a general consensus [24–28, 47] that this process is driven by instabilities such as the Crow, elliptic, and possibly the Kelvin-Helmholtz instabilities. At $t = 7.0$, the reconnection of the vortical structures triggers the onset of turbulence. Figure 5h illustrates the existence of regions featuring bursts of fine-scale turbulent flow. In the next instants, turbulence develops and extends throughout the domain as observed at $t = 9$ in the vicinity of $x_3 = \pi/2$. This result demonstrates that the turbulent field is not homogeneous due to its dependence on the vertical direction (x_3). At later times ($t \geq 12.0$), we can observe fine-scale turbulence in most of the computational domain which suggests fully-developed turbulent flow. This leads to the rapid dissipation of kinetic energy and flow structures observed in figures 5k to 5l ($t = 12 \rightarrow 20$).

The analysis of figure 5 also indicates the existence of two distinct periods in the development of the TGV flow: *i*) until $t = 9$, the flow is characterized by multiple coherent structures and instabilities which develop in time. This means the flow physics is governed by linear processes. Since turbulence constitutive relations are elastic rather than viscous in the linear regime, most practical one-point turbulence closures are expected to underperform during this period. *ii*) After $t = 9$, the flow exhibits fully-developed turbulence features which one-point closures can better model. Considering the properties of these two periods, it is expected that the prediction of the first nine time-units of the TGV flow poses challenges to modeling and simulation.

We now evaluate the performance of the proposed PANS method predicting the TGV flow, as well as the model's dependence on the physical resolution (f_k).

IV.2. Effect of physical resolution

The physical resolution of an SRS model dictates the range of resolved scales and, consequently, the efficiency (balance between accuracy and cost) of the computations. Whereas large physical resolutions may unnecessarily increase the computations' cost, reduced values of this parameter can compromise the accuracy of the predictions. Considering that the physical resolution of PANS BHR-2 is set through f_k ($f_\varepsilon = 1.00$), we investigate the dependence of the predictions' accuracy on this parameter. Toward this end, PANS calculations are conducted at six constant values of f_k : 0.00, 0.25, 0.35, 0.50, 0.75 and 1.00. Once again, recall that $f_k = 0.00$ is equivalent to not using a closure (DNS, if the resolution is sufficient), and $f_k = 1.00$ to RANS.

To illustrate the effect of f_k on the flow dynamics, figure 5 depicts the iso-surfaces of the vertical vorticity for different values of f_k . As expected, the results indicate that the range of resolved scales grows with $f_k \rightarrow 0$, this increasing the flow unsteadiness. Considering the limiting cases, the data show that the flow predicted at $f_k = 1.00$ is dominated by large-scale coherent structures, whereas fine-scale structures predominate at $f_k = 0.00$. Most notably, the absence of large-scale structures in the flow field obtained at $f_k = 0.00$ is evidence of significant morphological differences between the mean-flow field of these limiting cases.

The physical resolution also influences the numerical requirements of the simulations, such as the spatio-temporal grid resolution needed to predict the flow within a given level of numerical uncertainty, U_n . We emphasize that the quantification of U_n is crucial to gain confidence in the results and prevent misleading conclusions due to canceling between different components of the computational error [104]. To maintain the level of numerical uncertainty, the cost/grid resolution of the simulations is expected to increase with the physical resolution ($f_k \rightarrow 0$) owing to the resulting steeper gradients.

The numerical accuracy of the simulations at different values of f_k is evaluated in figure 7. This figure depicts the temporal evolution of the mean total flow kinetic energy, k_t ,

$$k_t = k_r + k_u \quad (53)$$

and respective numerical uncertainty, $U_n(k_t)$. Here, k_r and k_u are the resolved and unresolved/modeled components of k_t obtained from the resolved velocity field (k_r) and the closure (k_u). The black line in figure 7 represents the predicted $k_t(t)$, whereas the orange area $U_n(k_t)$ estimated with the procedure proposed by Eça and Hoekstra [107] using the solutions on three grid resolutions: the three coarsest grids for $f_k \geq 0.25$ ($N_c \leq 512^3$), and both the three coarsest and finest ($N_c \geq 256^3$) grids for $f_k = 0.00$. The numerical interpretation of U_n is the following. The unavailability of an exact solution for the present problem precludes calculating the simulations' discretization error. Instead, we estimate an uncertainty interval containing the exact solution of the mathemat-

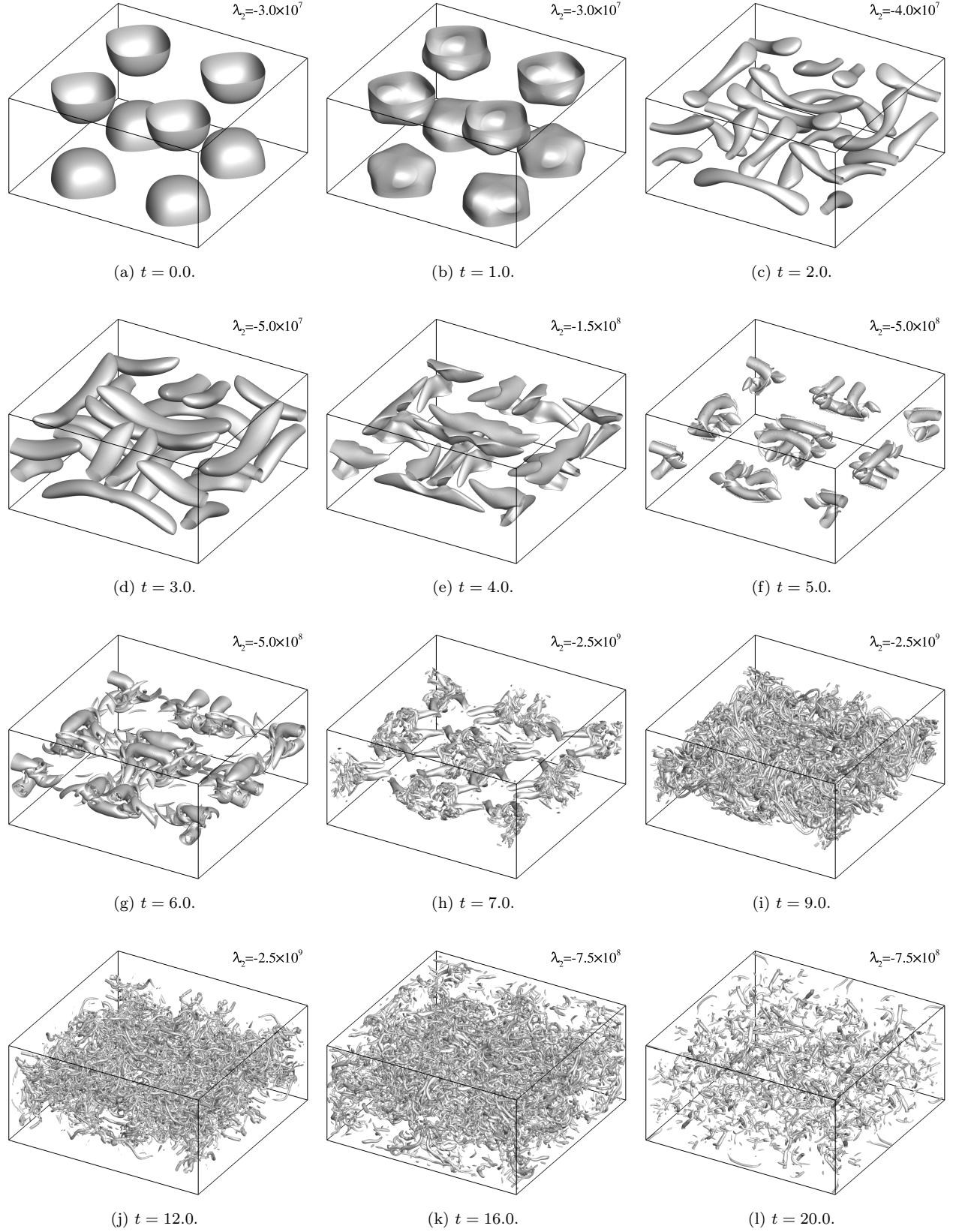


FIG. 5: Temporal evolution of the coherent and turbulent structures of the TG flow predicted with PANS using $f_k = 0.00$ and $N_c = 512^3$. Vortical structures identified with the λ_2 -criterion [102].

ical model within 95% confidence [107]. For the same grid, a reduction of U_n indicates smaller numerical er-

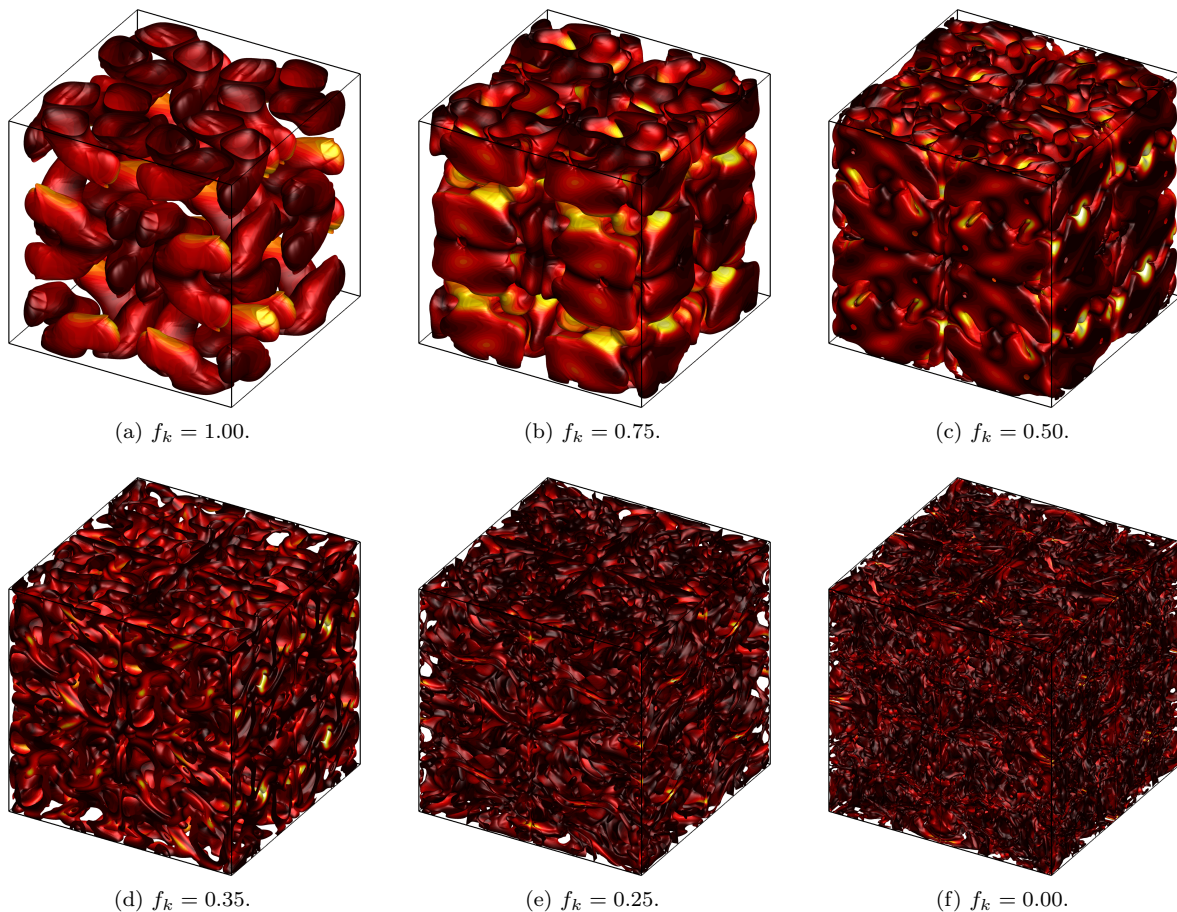


FIG. 6: Vertical vorticity, ω_3 , iso-surfaces colored by the normalized vorticity magnitude, $|\omega|$, for simulations using different values of f_k and $N_c = 512^3$. Results at $t = 20$.

rors. In figure 7, the height of the orange area shows the magnitude of U_n at a given time instant.

Referring to the simulations at $f_k \geq 0.50$, figures 7a-7c, these reveal reduced values of $U_n(k_t)$ for most of the simulated time. Taking the case of $f_k = 1.00$ (equivalent to RANS), the results show that the numerical uncertainty does not exceed 3.3% of the predicted value. The exceptions occur between $t = 6$ and 10 where $U_n(k_t)$ can reach a value of 10.8%. This growth originates in the use of the coarsest grid to estimate U_n and the fact that the onset and development of turbulence occur during this period. As discussed below, low-physical resolution ($f_k \geq 0.50$) simulations overpredict turbulence during the onset of turbulence. This stems from well-recognized limitations of one-point closures to predict this phenomenon and leads to a premature and rapid dissipation of k_t , which increases the steepness of the flow gradients. As a result, the numerical uncertainty increases in these time instants.

The refinement of physical resolution to $f_k = 0.35$ and 0.25, figures 7d-7e, causes a significant reduction of $U_n(k_t)$. For these cases, the numerical uncertainty does not exceed 8.7% of k_t at late times when the flow features high-intensity turbulence. In contrast, the further

refinement of physical resolution ($f_k = 0.00$) leads to a strong increase of $U_n(k_t)$ at $t > 11.0$, figure 7f. To understand this result, recall that during this period, the flow is characterized by high-intensity turbulence. Hence, formulations resolving all flow scales (DNS for $U_n \approx 0$; ILES for $U_n > 0$) are expected to be computationally more intensive than those at $f_k > 0.0$ predicting high-intensity turbulent flow. Results on the grid with 1024^3 cells confirm this idea by exhibiting similar values of $U_n(k_t)$ to those of PANS at $f_k = 0.25$ on $N_c = 512^3$. Nevertheless, $U_n(k_t)$ can still reach 8.4% at $t = 13$, whereas for $f_k = 0.25$ does not exceed 2.9%.

Overall, these numerical uncertainties enable the robust evaluation of the PANS model due to their reduced values. The results also demonstrate that to obtain similar numerical uncertainties, simulations at $f_k = 0.00$ require a minimum of $N_c = 1024^3$, whereas those at $f_k \leq 0.25$ relax the grid resolution requirement to $N_c = 512^3$. This is expected to have a significant impact on the computational resources required by the computations. It is important to emphasize that estimates using the coarsest grid, $N_c = 128^3$, should overpredict $U_n(\phi)$ due to the observed large discrepancies between solutions on this and the remaining grids (see Pereira et al. [108]).

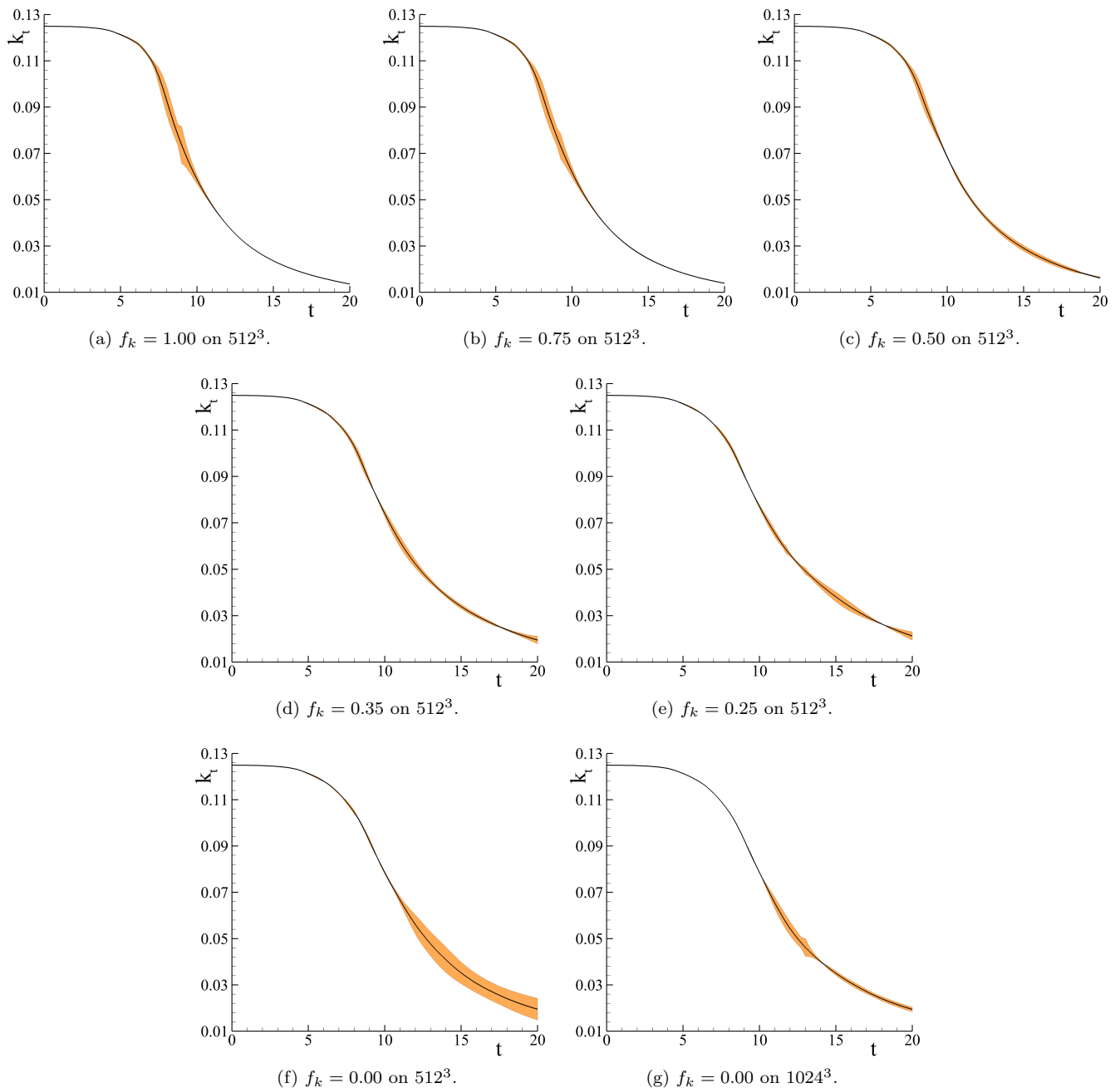


FIG. 7: Temporal evolution of the total kinetic energy, k_t , and respective numerical uncertainty, $U_n(k_t)$, for simulations using different values of f_k and grid resolutions.

Next, figure 8 presents the temporal evolution of k_t upon grid and physical resolution refinement. The grid resolution is here defined through the grid refinement ratio, r_i ,

$$r_i = \frac{\sqrt[3]{(N_c)_1}}{\sqrt[3]{(N_c)_i}}, \quad (54)$$

where the index i denotes the grid resolution with $i = 1$ referring to the finest grid resolution. At $t = 5$, figure 8a, the results of all PANS simulations converge monotonically upon grid refinement ($r_i \rightarrow 1$) and show that

the closure and physical resolution have a negligible impact on the solutions ($\tau^1(V_i, V_j) \approx 0$). At slightly later time, $t \geq 7$, the solutions start exhibiting an increasingly larger dependence on the physical resolution and convergence with f_k and r_i . Figures 8b-8d also evidence large discrepancies between low- ($f_k \geq 0.5$) and high- ($f_k < 0.50$) physical resolution simulations. Whereas low-physical resolution computations exhibit a strong dependence on f_k , high-physical resolution simulations are significantly less dependent on this parameter. This behavior has also been observed for transitional bluff-body

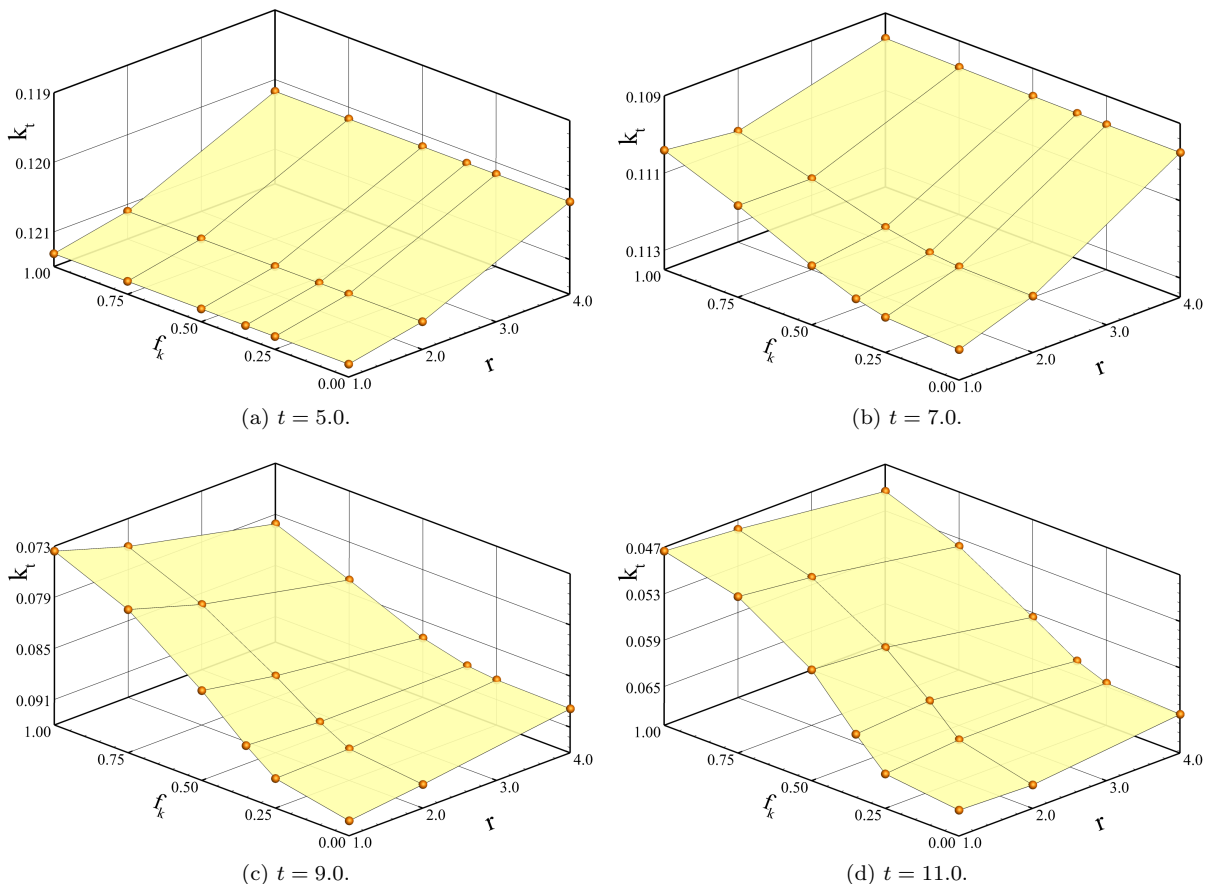


FIG. 8: Evolution of the total kinetic energy, k_t , with r_i and f_k for different time instants.

flows [12, 13, 76, 78].

Figure 9 depicts the temporal evolution of k_t for simulations conducted at different values of f_k on the finest grid resolution available ($N_c = 512^3$ or 1024^3). The numerical results of low- and high-physical resolution simulations are presented individually in figures 9a and 9b, respectively. Focusing on the low-physical resolution calculations, the results show that the simulations are independent of f_k until $t_c = t \approx 6$. After this instant, we observe a rapid decay of k_t (compared to $f_k < 0.50$) caused by the growth of the modeled turbulent stresses. Yet, it is essential to recall that *i*) the flow is expected to be laminar until $t \approx 7$ [47], and *ii*) the vortex-reconnection mechanism driving the onset of turbulence occurs between $t = t_c$ and 7 (figure 5). Between low-physical resolution computations, those performed at $f_k = 1.00$ and 0.75 predict similar temporal evolutions of k_t .

On the other hand, the results of high-physical resolution simulations are in close agreement, especially until $t = 10$. The discrepancies between different f_k 's do not exceed 0.0047. Compared to low-physical resolution computations, these simulations lead to slower decay rates of k_t and, consequently, to larger kinetic energy values. The results also show that the solutions do not converge monotonically with f_k after $t \approx 10$. We attribute this behavior to numerical uncertainty, especially for simula-

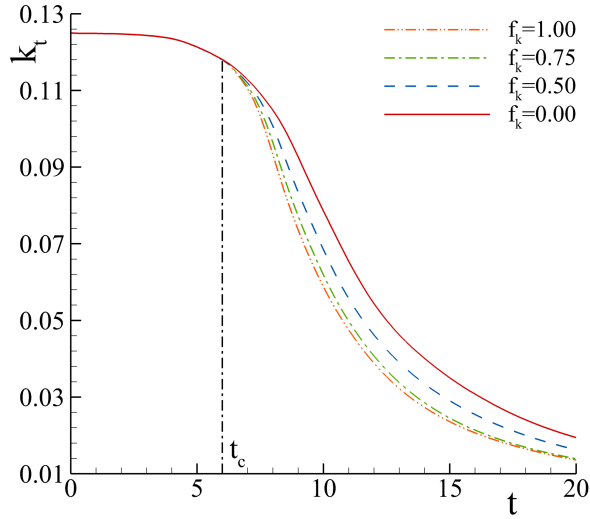
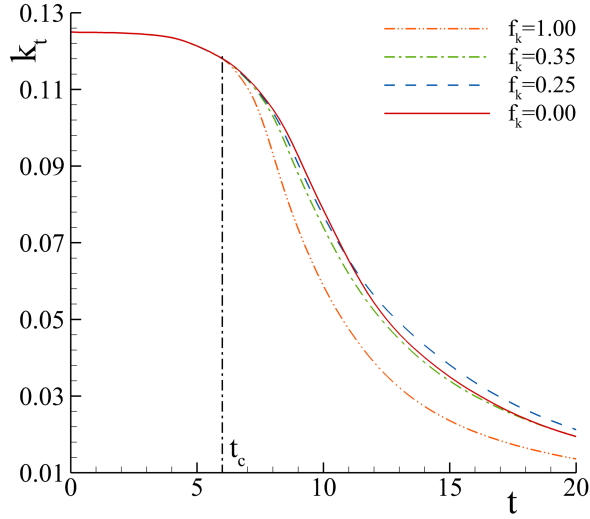
tions at $f_k = 0.00$.

Now, we turn our attention to the temporal evolution of the kinetic energy dissipation, ε_t ,

$$\varepsilon_t = -\frac{\partial k_t}{\partial t}, \quad (55)$$

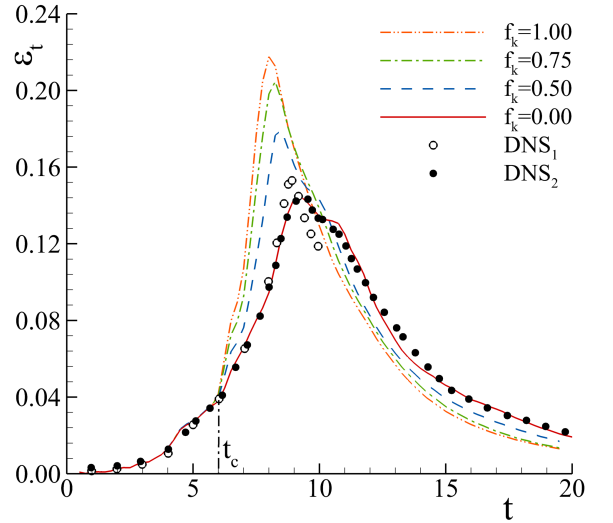
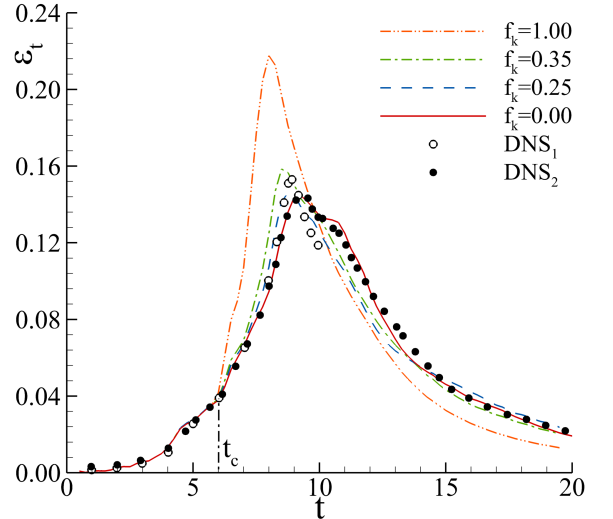
and its dependence on f_k . Figure 10 compares the predictions against the DNS of Brachet et al. [47] and Drikakis et al. [51]. As mentioned in [47, 51], these reference DNS simulations are likely underresolved at late times ($U_n > 0$) and were conducted at different Mach numbers (Ma). Whereas the simulations of Brachet et al. [47] are incompressible (Ma= 0), those of Drikakis et al. [51] are characterized by an initial $Ma_0 = 0.28$, which matches that of the present PANS calculations. Considering the differences in Ma and the study of Virk et al. [109], we can expect small discrepancies in ε_t between the two datasets.

The results of figure 10 illustrate that the predictions are independent of the physical resolution (f_k) until $t = t_c$. Recall that this is the moment when the vortex-reconnection process initiates (figure 5). After this time instant, low- ($f_k \geq 0.50$) and high- ($f_k < 0.50$) physical resolution computations exhibit distinct behaviors. Low-physical resolution simulations predict the peak of dissipation prematurely and overpredict its magnitude.

(a) k_t at $1.00 \leq f_k \leq 0.50$.(b) k_t at $0.35 \leq f_k \leq 0.00$.FIG. 9: Temporal evolution of the total kinetic energy, k_t , for simulations using different values of f_k .

These tendencies become more pronounced as the physical resolution is coarsened ($f_k \rightarrow 1.00$). For instance, it is observed that the peak of ε_t obtained at $f_k = 1.00$ can reach 0.218, whereas the reference DNS report values between 0.143 and 0.153 (values extracted graphically from [47, 51]). Compared to the value predicted by Drikakis et al. [51], this represents an increase of approximately 52.0%. Also, the maximum ε_t occurs at $t \approx 8$ for the simulation at $f_k = 1.00$, whereas the reference DNS report values between 9.0 and 9.3. These results suggest that low-physical resolution formulations lead to premature onset of turbulence and consequent turbulence overprediction, causing the rapid decay of k_t observed in figure 9a.

In contrast, high-physical resolution computations are in good agreement with the reference numerical experiments. For example, the results of the simulations at

(a) ε_t at $1.00 \leq f_k \leq 0.50$.(b) ε_t at $0.35 \leq f_k \leq 0.00$.FIG. 10: Temporal evolution of the total kinetic energy dissipation, $\varepsilon_t \times 10$, for simulations using different values of f_k .

$f_k \leq 0.25$ show that the maximum value of ε_t occurs at $t = 8.8 - 9.3$ and ranges from 0.145 to 0.146, whereas the DNS studies report $(\varepsilon_t)_{\max}$ between 0.143 and 0.153 at $t = 8.8 - 9.3$. The largest differences between PANS and DNS simulations occur at late times, $t > 10$. These small discrepancies are likely caused by numerical uncertainty and Ma effects.

IV.3. Physical interpretation of the results

The accuracy of the numerical results shows strong dependence on the physical resolution (f_k) of the model. Whereas high-physical resolution simulations ($f_k < 0.50$) reveal a good agreement with the DNS studies [47, 51], those performed at low-physical resolution ($f_k \geq 0.50$)

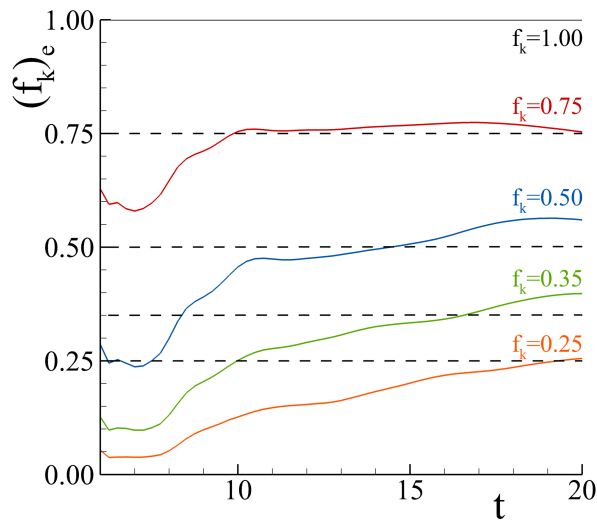


FIG. 11: Temporal evolution of the effective f_k , $(f_k)_e$, for simulations using different values of f_k .

lead to large discrepancies with the reference data. The modeling and physical reasons for this outcome are now examined.

IV.3.1. Effective ratio of modeled-to-total turbulent kinetic energy

In the PANS BHR-2 model, the physical resolution is set through the modeled-to-total ratio of turbulence kinetic energy f_k ($f_\varepsilon = 1.00$). Yet, this parameter may not match the effective f_k ,

$$(f_k)_e = \frac{k_u}{k_{u(f_k=1.00)}}, \quad (56)$$

of the simulations in cases where the closure misrepresents the turbulent kinetic energy field, e.g., problems characterized by massive flow separation or turbulence onset.

To analyze this aspect, figure 11 depicts the temporal evolution of $(f_k)_e$ for computations at different values of f_k . This figure only considers the period in which the solutions are dependent on f_k , $t \geq t_c$. The results indicate that $(f_k)_e$ is initially significantly smaller than the prescribed f_k (for cases at $f_k < 1.00$). This stems from the fact that the onset of turbulence delays with the refinement of f_k (see Section IV.3.3). After this period ($t > 8 - 9$), $(f_k)_e$ grows for all cases and gets closer to the prescribed value. Among all f_k , only the case at $f_k = 0.75$ converges toward the prescribed value during the simulated time. This is not observed for the remaining cases, highlighting that $f_k \neq (f_k)_e$ and reaffirming the dependence of the turbulent kinetic energy on the physical resolution.

Next, figure 12 depicts the ratio of unresolved-to-total kinetic energy, k_u/k_t , to assess the modeled fraction of k_t . The data show that k_u/k_t is nearly zero until $t = t_c$.

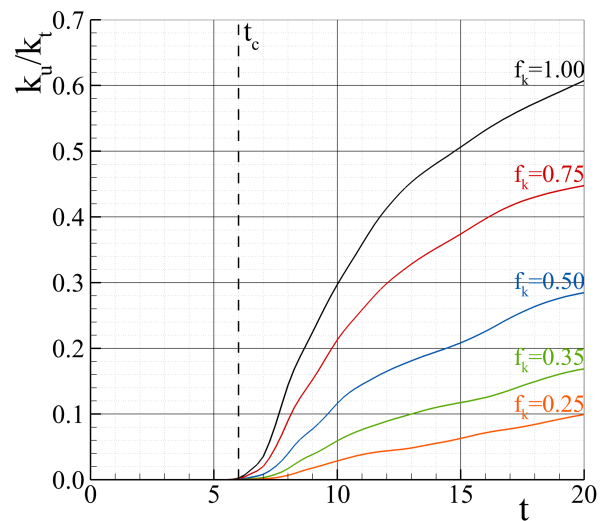


FIG. 12: Temporal evolution of the ratio modeled-to-total kinetic energy, k_u/k_t , for simulations using different values of f_k .

This explains the observed independence of k_t and ε_t solutions (figures 9 and 10) from f_k . After this instant, this quantity presents a rapid growth, which rate is closely dependent on f_k . Also, and considering the two periods of the development of the TGV flow (see Section IV.1), it is possible to infer the following: *i*) during the first period, $t \leq 9$, the magnitude of k_u is relatively small compared to k_t . This indicates that even small fractions of k' have a strong impact on the flow physics and accuracy of the simulations. *ii*) At later times, $t > 9$, the contribution of k_u grows significantly. Nevertheless, at $t = 20$, k_u/k_t still does not exceed 16.9% and 60.8% for simulations using $f_k = 0.35$ and 1.00, respectively.

From a modeling perspective, the most significant result of figure 12 is the fact that k_u/k_t predicted with $f_k = 1.00$ is approximately six times larger than at $f_k = 0.25$. This outcome is caused by the early onset and overprediction of turbulence by low-physical resolution simulations. It is also interesting to note that the ratio k_u/k_t for high-physical resolution simulations only starts increasing at $t \geq 7$, i.e., after the vortex-reconnection processes observed in figure 5. Recall that this is the time instant when we first observe bursts of turbulence.

IV.3.2. Effective Reynolds number

One of the main consequences of modeling the turbulent field is the inherent reduction of the effective Reynolds number, Re_e ,

$$Re_e \equiv \frac{V_o L_o}{\nu + \nu_u}, \quad (57)$$

of the computations. Although lower physical resolutions reduce this quantity and relax the simulations' cost, an excessively large decrease of Re_e may compromise the

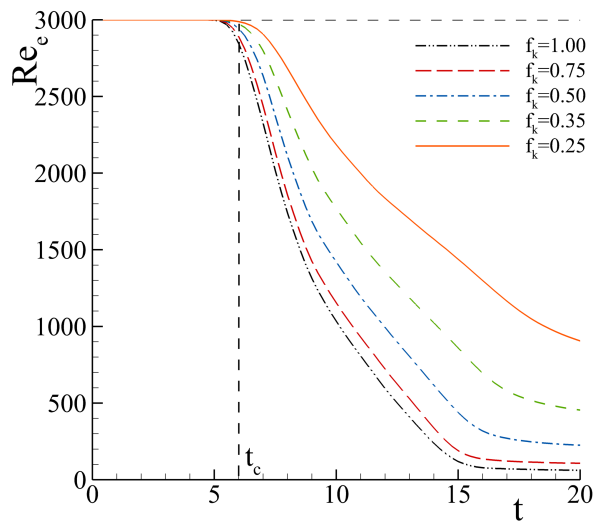


FIG. 13: Temporal evolution of the effective Reynolds number, Re_e , for simulations using different values of f_k .

accuracy of the simulations. Pereira et al. [12, 13, 76] demonstrated the importance of this quantity to the prediction of flows around circular cylinders in the sub-critical regime [10, 11]. These studies show that an excessive reduction of Re_e can suppress the instabilities and coherent structures driving the flow dynamics, leading to poor results. Since the TGV flow exhibits a strong dependence on the magnitude of Re [47], we now evaluate the effect of the physical resolution on Re_e .

The temporal evolution of Re_e is depicted in figure 13 for different values of f_k . The results show that this quantity is independent of the physical resolution until $t = 5$. Also, only high-physical resolution simulations maintain $Re_c \approx 3000 = Re$ until $t = t_c$. After this instant, the magnitude of Re_e experiences a rapid decay, which is particularly pronounced for low-physical resolution simulations. The results also show that the beginning and steepness of the Re_e reduction depends on f_k . For example, it is observed that the averaged value of Re_e at $t = 9$ is equal to 2033 and 1313 for simulations at $f_k = 0.35$ and 1.00, respectively. At later times, $t > 15$, Re_e starts becoming independent of time. This stems from a nearly constant averaged value of ν_u , which suggests that the turbulent field is becoming fully-developed. These features occur later as the physical resolution refines.

IV.3.3. Coherent field

Section IV.1 has shown that the development of the TGV flow comprises two distinct periods. In the first, the flow evolves from a laminar to a turbulent state, driven by multiple coherent structures and instabilities. On the other hand, the second period is characterized by fully-developed, high-intensity, and decay of turbulence. Comparing the features of the two periods, it is possible to infer that the first poses more challenges to

modeling and simulation. The numerical results have confirmed this idea by showing that the discrepancies between simulations at different physical resolutions begin at $t = t_c$. This instant coincides with the onset of vortex-reconnection.

To investigate the origin of these discrepancies, figures 14-16 depict the main coherent structures observed at $t_c \leq t \leq 7.0$ and different values of f_k . These vortical structures are identified through the iso-surfaces of the λ_2 -criterion [102] ($\lambda_2 = -2.5 \times 10^9$) and colored by the magnitude of the turbulent-to-molecular kinematic viscosity ratio, ν_u/ν . The maximum values of ν_u/ν obtained at each time instant and f_k are presented in table III. Referring to the computations at $f_k \leq 0.25$, figure 14, we observe that the coherent field predicted at these physical resolutions exhibits similar features. The plot shows that orthogonal pairs of counter-rotating vortices interact and reconnect, this leading to the onset of turbulence at $t = 7.0$ (bursts of fine-scale turbulence). Also, table III indicates that $(\nu_u/\nu)_{\max}$ is small and does not exceed 0.25 at $t = 6.0$, 1.08 at $t = 6.5$, and 1.30 at $t = 7.0$. Figure 15 illustrates that coarsening the physical resolution to $f_k = 0.50$ has a strong impact on the predicted coherent field. Whereas the simulation at $f_k = 0.35$ can capture the vortical structures observed at $f_k \leq 0.25$ and exhibits mild levels of $(\nu_u/\nu)_{\max}$ not exceeding 2.9, the computation at $f_k = 0.50$ leads to significant morphological changes of the coherent field. At $t = 7.0$, figure 15f, part of the coherent field has been dissipated through the overprediction of turbulence and ν_u/ν . It is observed that ν_u can exceed its molecular counterpart by 1.7 times at $t = 6.0$, 6.3 at $t = 6.5$, and 6.6 at $t = 7.0$. As f_k further coarsens, figure 16, these phenomena become more pronounced. Taking the case of $f_k = 1.00$, the corresponding figures show that the coherent field is strongly affected at $t = 6.50$, and a significant fraction of the laminar vortical structures has been dissipated by the large values of ν_u/ν . Table III indicates that this quantity can reach 4.4 at $t = 6$.

Yet, the most significant result in figures 14-16 is the fact that it demonstrates that the accuracy of the simulations is determined by their ability to capture the vortical structures responsible for the onset of turbulence. Thus, the results reaffirm the findings of Pereira et al. [12]. These indicate that efficient SRS calculations require the selection of the smallest physical resolution that enable the model to resolve only the flow scales not amenable to modeling (most of the coherent field). For the simulation of the TGV with PANS BHR-2, this objective can

TABLE III: Maximum value of the turbulent-to-molecular viscosity, $(\nu_u/\nu)_{\max}$, registered for different instants and values of f_k .

t	0.00	0.25	0.35	0.50	0.75	1.00
6.0	0.0	0.3	0.7	1.7	4.4	8.6
6.5	0.0	1.1	2.7	6.3	16.0	30.1
7.0	0.0	1.3	2.9	6.6	17.8	35.5

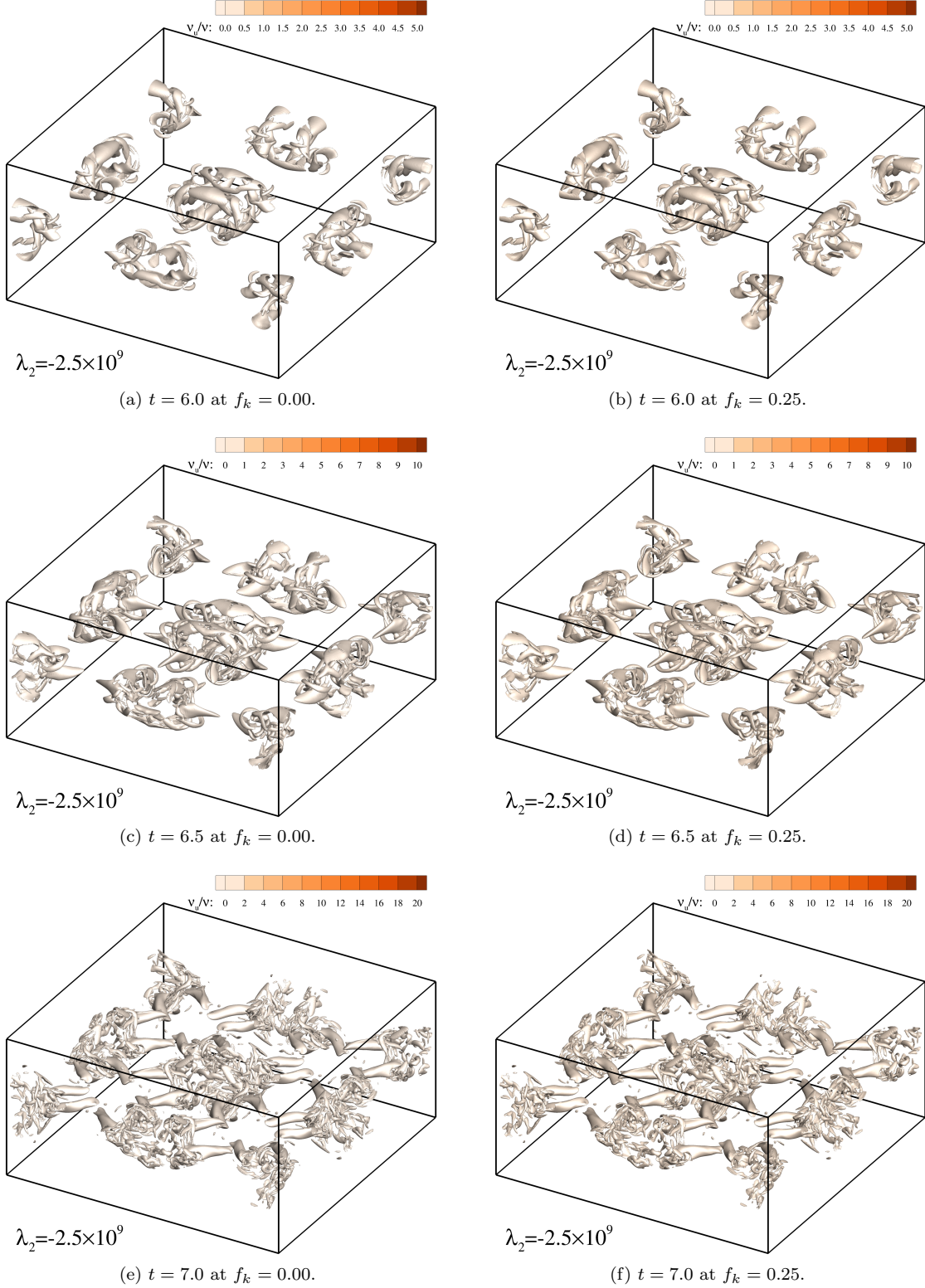


FIG. 14: Temporal evolution of the vortical structures of the TGW flow for simulations at $f_k = 0.00$ and 0.25 . Structures captured with λ_2 -criterion [102].

be achieved by setting f_k between 0.25 and 0.35 .

IV.3.4. Spectral features

Next, we turn our attention to the effect of the physical resolution on the spectral features of the TGW flow.

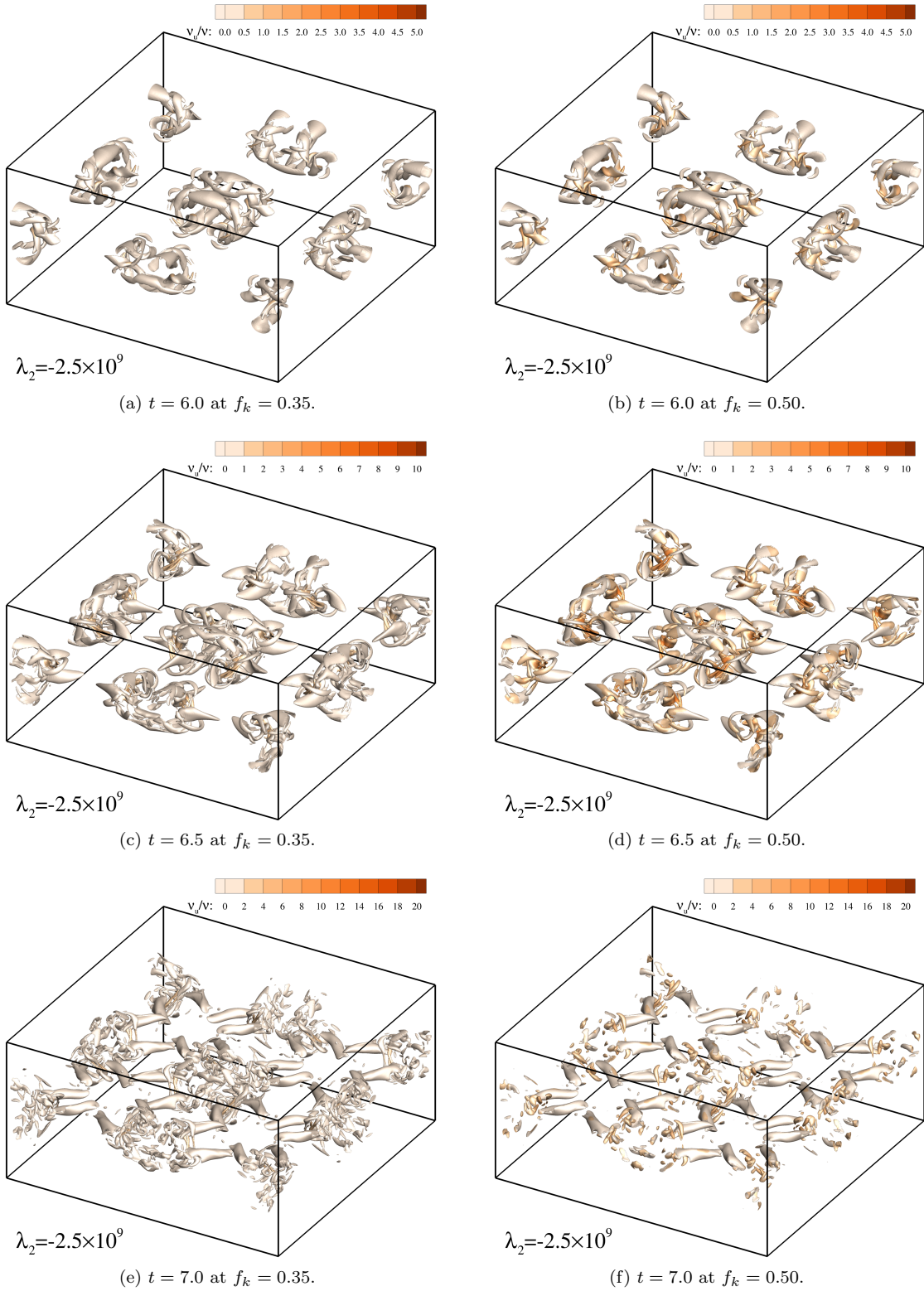


FIG. 15: Temporal evolution of the vortical structures of the TG flow for simulations at $f_k = 0.35$ and 0.50 . Structures captured with λ_2 -criterion [102].

Figure 17 depicts the velocity spectra of the simulations at successively later time instants and different physical resolutions, f_k . The spectra obtained from

high-physical resolution computations include an inertial range, in which the physical resolution determines the largest wavelength. As expected, it is observed that refin-

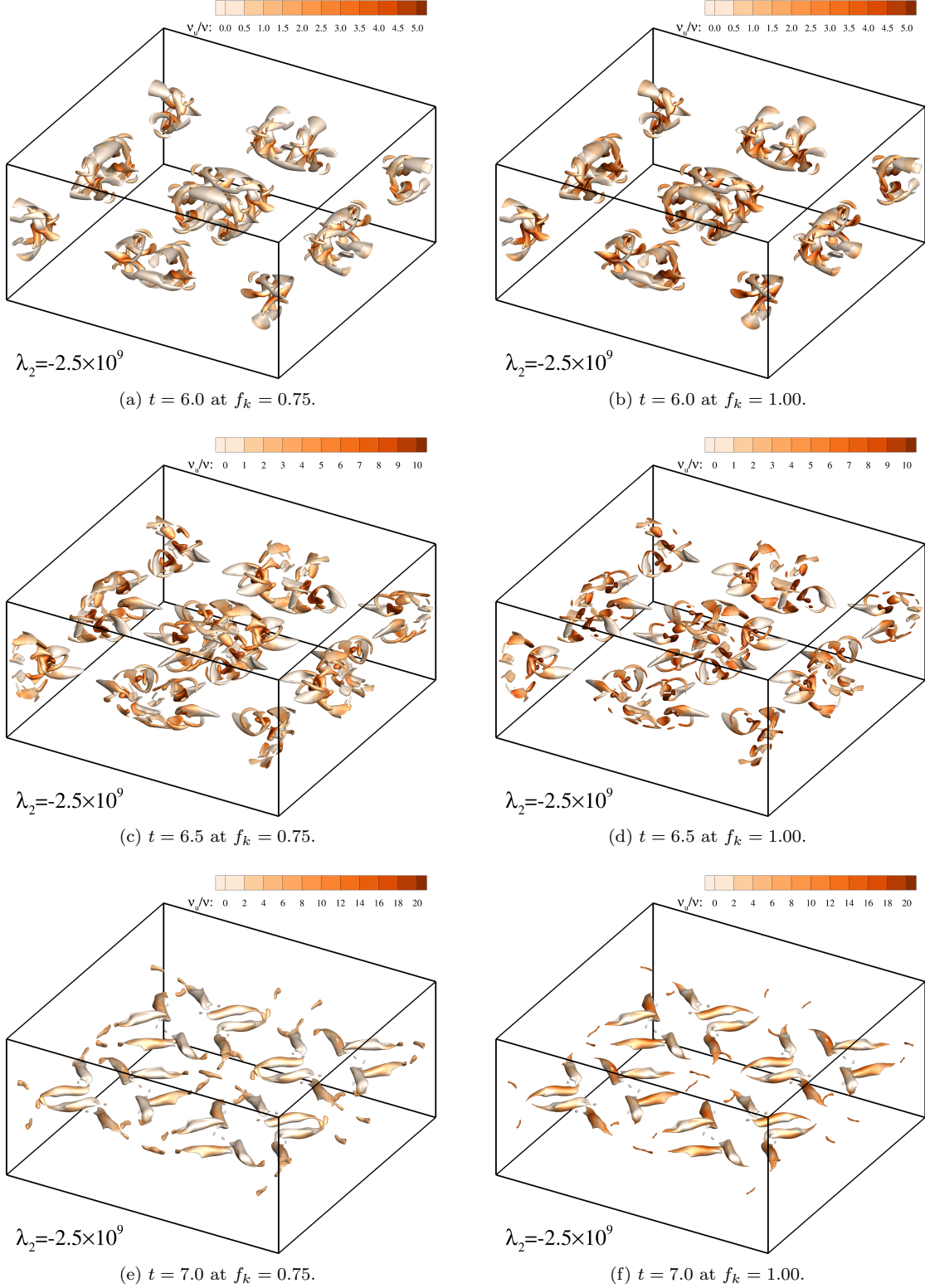


FIG. 16: Temporal evolution of the vortical structures of the TG flow for simulations at $f_k = 0.75$ and 1.00 . Structures captured with λ_2 -criterion [102].

ing f_k leads to longer inertial ranges but does not significantly affect the large, energy-containing scales; only the simulation at $f_k = 0.00$ resolves the viscous scales (vis-

ous sub-range). Considering the results of this study, this demonstrates that it is possible to obtain accurate simulations without resolving all/most turbulent scales.

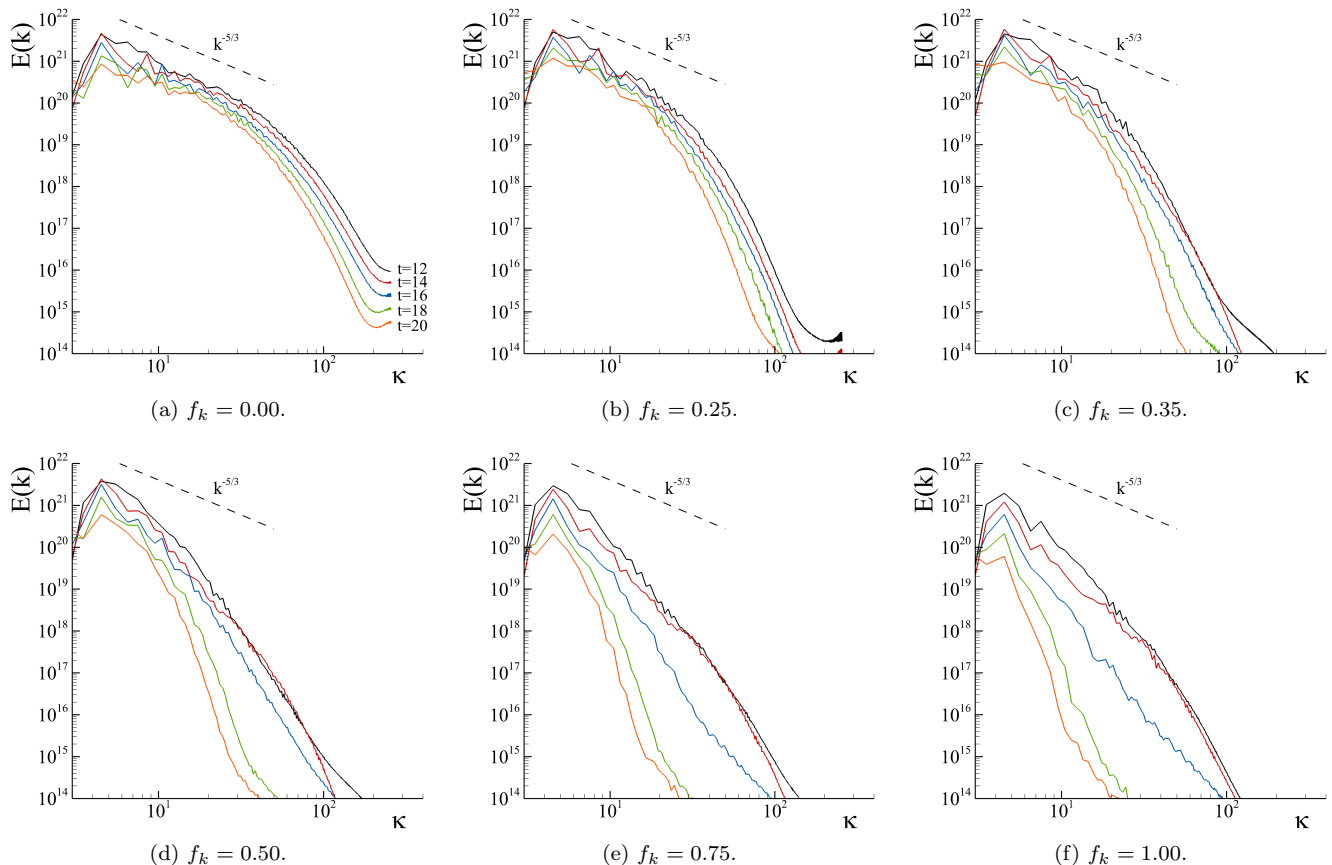


FIG. 17: Temporal evolution of the turbulence kinetic energy spectrum, $E(k)$, for simulations using different values of f_k .

In contrast, the spectra obtained from low-physical resolution simulations are characterized by lower energy levels across the entire spectrum, including significant damping of the large-scale structures. Along with the reduced physical resolution, this result stems from the premature onset and overprediction of turbulence. For all values of f_k , it is possible to observe that the kinetic energy decreases with time. Yet, the decay rate increases with f_k .

IV.4. Computational cost

The discussion of the results concludes with the evaluation of the simulations' computational intensity. Table IV presents the cost in CPU.hours of the computations on different grid resolutions (N_c) and physical resolutions (f_k). Unfortunately, we cannot show the exact value for the cost of the simulations on $N_c = 1024^3$. In this case, we present a very conservative estimate based on the cost of the computations on the grids with 256^3 and 512^3 cells.

As expected, table IV shows that the computational cost of the simulations grows upon grid refinement. The results show that doubling the grid resolution increases the cost of the computations by more than one order of

magnitude. Taking the case of $f_k = 0.00$, the number of CPU.h grows 14.9 times from simulations on $N_c = 128^3$ to 256^3 , and 17.9 times from $N_c = 256^3$ to 512^3 . On the other hand, the comparison of the simulations' cost at different physical resolutions presents two distinct behaviors. First, computations resolving all flow scales ($f_k = 0.00$) are computationally less intensive than the remaining. For the same grid, we obtain savings that can reach 20.8%. This reflects the cost of computing the closure model. Second, the cost of simulations at $f_k > 0.00$ grows with the physical resolution. This is caused by the broader range of resolved scales that increases the steepness of the flow gradients (affecting iterative solvers' performance) and the implicit contribution of closure's discrete system of equations [104, 110, 111].

Although simulations at $f_k = 0.00$ are computationally less intense than those at $f_k > 0.00$ on the same grid, they require finer grid resolutions to obtain the same level of numerical uncertainty (a measure of the numerical error). The data show that computations at $f_k = 0.00$ require a grid with a minimum of $N_c = 1024^3$ cells to obtain similar magnitudes of numerical uncertainty as $f_k = 0.25$ using $N_c = 512^3$. This leads to a significant reduction of the simulations' cost from 5,782,595 to 406,803 CPU.h, which illustrates the potential of PANS method to predict the present transitional flow efficiently.

TABLE IV: Computational cost (CPU.hours) of PANS simulations at different values of f_k and grid resolutions. * indicates extrapolated value.

f_k	0.00	0.25	0.35	0.50	0.75	1.00
$N_c = 1024^3$	5,782,595*	–	–	–	–	–
$N_c = 512^3$	322,284	406,803	405,435	400,139	393,947	398,927
$N_c = 256^3$	17,962	21,600	21,408	21,431	21,216	20,916
$N_c = 128^3$	1,204	1,392	1,375	1,336	1,321	1,320

V. CONCLUSIONS

A new PANS model is used to predict the transitional TGV flow at $Re = 3000$. This is an archetypal problem widely utilized to assess the performance of turbulence models simulating transitional flows driven by vortex-stretching and reconnection mechanisms. Since these phenomena are present in numerous flows of variable-density (e.g., ocean and mixing problems), this work constitutes the first step toward extending PANS to this class of flows.

The study starts by deriving the governing equations of the model. This includes the assessment of the parameters controlling the physical resolution of the model, f_k and f_ε , and their dependence from the range of resolved scales. It is shown that the usual assumption of setting $f_\varepsilon = 1.00$ is acceptable for values of f_k of practical interest ($f_k \geq 0.20$). For this reason, all simulations are conducted using $f_\varepsilon = 1.00$. In regard to f_k , we use different constant values of this parameter to evaluate the effect of the physical resolution on the simulations. This approach also prevents commutation errors, and enables robust verification and validations exercises since the governing equations of the model do not depend on the grid resolution.

The discussion of the results is preceded by a qualitative analysis of the flow dynamics and vortical structures using the simulation at $f_k = 0.00$. It is inferred that the development of the TGV flow comprises two distinct periods: *i*) in the first, the initially well-defined laminar vortices interact and deform, leading to the onset and development of turbulence through vortex-stretching and reconnection mechanisms. *ii*) in the second, the flow exhibits high-intensity turbulence features and experiences a rapid decay of kinetic energy due to turbulent viscous dissipation.

The results of PANS simulations demonstrate that the model can efficiently predict the TGV flow. Yet, the computations' accuracy is closely dependent on the physical resolution, and, most notably, on the ability to predict the first stage of the flow development ($t \leq 9$). Whereas low-physical resolution ($f_k \geq 0.50$) simulations lead to poor representations of the flow dynamics, high-physical

resolution ($f_k < 0.50$) computations can accurately predict the TGV. The physical and modeling interpretation of the results indicates that the simulations' accuracy is determined by the ability to represent the vortex-reconnection mechanism driving the onset of turbulence. It is observed that low-physical resolution simulations overpredict turbulence, leading to the dissipation of these coherent structures and consequent poor representation of the flow physics. In contrast, high-physical resolution computations ($f_k < 0.50$) can accurately simulate these phenomena and, consequently, the flow physics. Regarding the computations' cost, the numerical uncertainty of the results indicates that simulations at $f_k = 0.00$ (equivalent to ILES since $U_n > 0$) require grids two times finer to obtain values of numerical uncertainty similar to those obtained by simulations at $f_k > 0$. Considering that all high-physical resolution computations can accurately predict the flow physics, the results illustrates that PANS ($0.25 \leq f_k \leq 0.35$) leads to cost savings exceeding one order of magnitude. These are expected to increase with Re .

In summary, this study reinforces the potential of the PANS method to calculate transitional flows of practical interest efficiently. Also, it reiterates that the success of SRS methods depends upon three important factors: *i*) ability to identify key flow mechanisms and coherent structures; *ii*) determining the optimum range of resolution required to predict the coherent field adequately; and *iii*) ensuring that the modeled flow field is comprised nearly exclusively of fully-developed stochastic turbulence [12].

ACKNOWLEDGMENTS

The authors would like to thank C. B. da Silva for sharing his DNS data sets and insightful discussions.

Los Alamos National Laboratory (LANL) is operated by TRIAD National Security, LLC for the US DOE NNSA. This research was funded by LANL Mix and Burn project under the DOE ASC, Physics and Engineering Models program. We express our gratitude to the ASC program and the High-Performance Computing (HPC) division for their dedicated and continued support of this work.

-
- [1] P. Dimotakis, Turbulent Mixing, *Annual Reviews of Fluids Mechanics* **37**, 329 (2005).
- [2] W. Cabot and A. Cook, Reynolds number effects on Rayleigh-Taylor instability with Possible Implications for Type Ia Supernovae, *Nature Physics* **2**, 562 (2006).
- [3] G. Orlicz, S. Balasubramanian, P. Vorobieff, and K. Prestidge, Mixing Transition in a Shocked Variable-Density Flow, *Physics of Fluids* **27** (2015).
- [4] F. Marble, G. Hendricks, and E. Zukoski, Progress Toward Shock Enhancement of Supersonic Combustion Processes, in *23rd American Institute of Aeronautics and Astronautics (AIAA) Joint Propulsion Conference*, AIAA-87-1880 (San Diego, United States of America, 1987) pp. 123-129.
- [5] J. Yang, T. Kubota, and E. E. Zukoski, Applications of Shock-Induced Mixing to Supersonic Combustion, *American Institute of Aeronautics and Astronautics Journal* **31**, 854 (1993).
- [6] Q. Yang, J. Chang, and W. Bao, Richtmyer-Meshkov Instability Induced Mixing Enhancement in the Scramjet Combustor with a Central Strut, *Advances in Mechanical Engineering* **6** (2014).
- [7] W. Arnett, J. Bahcall, and S. Kirshner, R.P. Woosley, Supernova 1987A, *Annual Reviews of Astronomy and Astrophysics* **629-700**, 213 (1989).
- [8] N. Hammer, H.-T. Janka, and E. Müller, Three-Dimensional Simulations of Mixing Instabilities in Supernova Explosions, *The Astrophysical Journal* **714**, 1371 (2010).
- [9] V. A. Thomas and R. J. Kares, Drive Asymmetry and the Origin of Turbulence in an ICF Implosion, *Physical Review Letters* **109** (2012).
- [10] C. H. K. Williamson, Vortex Dynamics in the Cylinder Wake, *Annual Review of Fluid Mechanics* **28**, 477 (1996).
- [11] M. M. Zdravkovich, *Flow Around Circular Cylinders. Volume 1: Fundamentals*, 1st ed. (Oxford Science Publications, Oxford, United Kingdom, 1997).
- [12] F. S. Pereira, L. Eça, G. Vaz, and S. S. Girimaji, Challenges in Scale-Resolving Simulations of Turbulent Wake Flows with Coherent Structures, *Journal of Computational Physics* **363**, 98 (2018).
- [13] F. S. Pereira, L. Eça, G. Vaz, and S. S. Girimaji, On the Simulation of the Flow Around a Circular Cylinder at $Re=140,000$, *International Journal of Heat and Fluid Flow* **76**, 40 (2019).
- [14] M. V. Morkovin, *Recent Insight into Instability and Transition to Turbulence in Open-Flow Systems*, techreport 88-44 (NASA - Langley Research Center, Hampton, Virginia, USA, 1988).
- [15] S. Kida and M. Takaoka, Vortex Reconnection, *Annual Reviews of Fluid Mechanics* **26**, 169 (1994).
- [16] T. E. Zaki, From Streaks to Spots and on to Turbulence: Exploring the Dynamics of Boundary Layer Transition, *Flow, Turbulence and Combustion* **91**, 451 (2013).
- [17] B. Eckhardt, Transition to Turbulence in Shear Flows, *Physica A* **504**, 121 (2018).
- [18] H. von Helmholtz, On Discontinuous Movements of Fluids, *The London, Edinburgh, and Dublin Philosophical Magazine and Journal of Science* **36**, 337 (1868).
- [19] W. Thomson, *Hydrokinetic Solutions and Observation*, *The London, Edinburgh, and Dublin Philosophical Magazine and Journal of Science* **42**, 362 (1871).
- [20] L. Rayleigh, Investigation of the Character of the Equilibrium of an Incompressible Heavy Fluid of Variable Density, *Proceedings of the London Mathematical Society* **14**, 170 (1882).
- [21] G. Taylor, The Instability of Liquid Surfaces when Accelerated in a Direction Perpendicular to their Planes, *Proceeding of the Royal Society A* **201**, 192 (1950).
- [22] R. Richtmyer, Taylor Instability in Shock Acceleration of Compressible Fluids, *Communications on Pure and Applied Mathematics* **13**, 297 (1960).
- [23] E. Meshkov, Instability of the Interface of Two gases Accelerated by a Shock Wave, *Soviet Fluid Dynamics* **4**, 151 (1969).
- [24] S. C. Crow, Stability Theory for a Pair of Trailing Vortices, *American Institute of Aeronautics and Astronautics (AIAA) Journal* **8**, 2172 (1970).
- [25] F. Laporte and T. Leweke, Elliptic Instability of Counter-Rotating Vortices: Experiment and Direct Numerical Simulation, *American Institute of Aeronautics and Astronautics (AIAA) Journal* **40**, 2483 (2002).
- [26] J. Yao and F. Hussain, Separation Scaling for Viscous Vortex Reconnection, *Journal of Fluid Mechanics Rapids* **900** (2020).
- [27] T. Leweke and C. Williamson, Cooperative Elliptic Instability of a Vortex Pair, *Journal of Fluid Mechanics* **360**, 85 (1998).
- [28] T. Leweke, S. L. Dizés, and C. H. K. Williamson, Dynamics and Instabilities of Vortex Pairs, *Annual Review of Fluid Mechanics* **48**, 507 (2016).
- [29] J. Smagorinsky, General Circulation Experiments with the Primitive Equations I. The Basic Experiment, *Monthly Weather Review* **91**, 99 (1963).
- [30] J. P. Boris, F. F. Grinstein, E. S. Oran, and R. L. Kolbe, New Insights into Large Eddy Simulation, *Fluid Dynamics Research* **10**, 199 (1992).
- [31] F. F. Grinstein, L. G. Margolin, and W. J. Rider, *Implicit Large Eddy Simulation: Computing Turbulent Flow Dynamics*, 2nd ed. (Cambridge University Press, New York, United States of America, 2010).
- [32] P. R. Spalart, W.-H. Jou, M. Strelets, and S. R. Allmaras, Comments on the Feasibility of LES for Wings, and on a Hybrid RANS/LES Approach, in *Proceedings of the 1st Air Force Office of Scientific Research (AFOSR) International Conference on DNS/LES* (Ruston, United States of America, 1997).
- [33] P. R. Spalart, Strategies for Turbulence Modelling and Simulations, *International Journal of Heat and Fluid Flow* **21**, 252 (2000).
- [34] F. R. Menter, J. Schütze, and K. A. Kurbatskii, Scale-Resolving Simulation Techniques in Industrial CFD, in *Proceedings of the 6th American Institute of Aeronautics and Astronautics (AIAA) Theoretical Fluid Mechanics Conference* (AIAA 2011-3474, Honolulu, United States of America, 2011).
- [35] D. C. Wilcox, *Turbulence Modeling for CFD*, 3rd ed. (DCW Industries, La Cañada, United States of America, 2006).
- [36] J. Piquet, *Turbulent Flows - Models and Physics*, 2nd ed. (Springer-Verlag, Berlin, Germany, 1999).
- [37] S. B. Pope, *Turbulent Flows*, 1st ed. (Cambridge University Press, Cambridge, United Kingdom, 2000).

- [38] K. Hanjalić and B. Launder, *Modelling Turbulence in Engineering and the Environment. Second-Moment Routes to Closure*, 1st ed. (Cambridge University Press, Cambridge, United Kingdom, 2011).
- [39] C. G. Speziale, Computing Non-Equilibrium Turbulent Flows With Time-Dependent RANS and VLES, in *15th International Conference on Numerical Methods in Fluid Dynamics*, Lecture Notes in Physics, Vol. 490, edited by P. Kutler and J. F. J. Chattot (Springer, Berlin, Germany, 1997).
- [40] H. F. Fasel, J. Seidel, and S. Wernz, A Methodology for Simulations of Complex Turbulent Flows, *Journal of Fluids Engineering* **124**, 993 (2002).
- [41] S. S. Girimaji, Partially-Averaged Navier-Stokes Model for Turbulence: A Reynolds-Averaged Navier-Stokes to Direct Numerical Simulation Bridging Method, *Journal of Applied Mechanics* **73**, 413–421 (2005).
- [42] R. Schiestel and A. Dejoan, Towards a New Partially Integrated Transport Model for Coarse Grid and Unsteady Turbulent Flow Simulations, *Theoretical and Computational Fluid Dynamics* **18**, 443 (2005).
- [43] B. Chaouat and R. Schiestel, A New Partially Integrated Transport Model for Subgrid-Scale Stresses and Dissipation Rate for Turbulent Developing Flows, *Physics of Fluids* **17** (2005).
- [44] *Transition Modeling Workshop 2017* (NASA, Suffolk, Virginia, USA, 2017).
- [45] *1st AIAA CFD Transition Modeling and Prediction Workshop* (AIAA, Reno, Nevada, USA, 2020).
- [46] G. I. Taylor and A. E. Green, Mechanism of the Production of Small Eddies from Large Ones, *Proceedings of the Royal Society A* **158** (1937).
- [47] M. E. Brachet, D. I. Meiron, S. A. Orzag, B. G. Nickel, R. H. Morf, and U. Frisch, Small Scale Structure of the Taylor-Green Vortex, *Journal of Fluid Mechanics* **130**, 411 (1983).
- [48] Y. Yang and D. I. Pullin, Evolution of Vortex-Surface Fields in Viscous Taylor-Green and Kida-Pelz Flows, *Journal of Fluid Mechanics* **685**, 146 (2011).
- [49] M. E. Brachet, Direct Simulation of Three-Dimensional Turbulence in the Taylor-Green Vortex, *Fluid Dynamics Research* (1991).
- [50] C.-W. Shu, W.-S. Don, D. Gottlieb, O. Schilling, and L. Jameson, Numerical Convergence Study of Nearly Incompressible, Inviscid Taylor–Green Vortex Flow, *Journal of Scientific Computing* **24**, 1 (2005).
- [51] D. Drikakis, C. Fureby, F. F. Grinstein, and D. Youngs, Simulation of Transition and Turbulence Decay in the Taylor-Green Vortex, *Journal of Turbulence* **8** (2007).
- [52] Y. Yang and D. I. Pullin, On Lagrangian and Vortex-Surface Fields for Flows with Taylor-Green and Koda-Pelz Initial Conditions, *Journal of Fluid Mechanics* **661**, 446 (2010).
- [53] J.-B. Chapelier, M. Plata, and F. Renac, Inviscid and Viscous Simulations of the Taylor-Green Vortex Using a Model Discontinuous Galerkin Approach, in *42nd American Institute of Aeronautics and Astronautics (AIAA) Fluid Dynamics Conference and Exhibit*, AIAA 2012-3073 (New Orleans, USA, 2012).
- [54] J. DeBonis, *Solutions of the Taylor-Green Vortex Problem Using High-Resolution Explicit Finite Difference Methods*, techreport NASA/TM-2013-217850 (National Aeronautics and Space Administration (NASA), Glenn Research Center, Cleveland, USA, 2013).
- [55] I. A. Shirokov and T. G. Elizarova, Simulation of Laminar-Turbulent Transition in Compressible Taylor-Green Flow Basing on Quasi-Gas Dynamic Equation, *Journal of Turbulence* **15**, 707 (2014).
- [56] J. R. Bull and A. Jameson, Simulation of the Taylor-Green Vortex using high-Order Flux Reconstruction Schemes, *American Institute of Aeronautics and Astronautics (AIAA) Journal* **53**, 2750 (2015).
- [57] T. Dairay, E. Lamballais, S. Laizet, and J. C. Vassiliocos, Numerical Dissipation vs. Subgrid-Scale Modelling for Large Eddy Simulation, *Journal of Computational Physics* **337**, 252 (2017).
- [58] R. E. Moura, G. Mengaldo, and J. P. amd S. J. Sherwin, On the Eddy-Resolving Capability of High-Order Discontinuous Galerkin Approaches to Implicit LES/Under-Resolved DNS of Euler Turbulence, *Journal of Computational Physics* **330**, 615 (2017).
- [59] N. Peng and Y. Yang, Effects of the Mach Number on the Evolution of Vortex-Surface Fields in Compressible Taylor-Green Flows, *Physical Review Fluids* **3** (2018).
- [60] N. Sharma and T. K. Sengupta, Vorticity Dynamics of the Three-Dimensional Taylor-Green Vortex Problem, *Physics of Fluids* **31** (2019).
- [61] F. F. Grinstein, J. A. Saenz, J. C. Dolence, T. O. Masser, R. M. Rauenzahn, and M. M. Francois, Effects of Operator Splitting and Low Mach-Number Correction in Turbulent Mixing Transition Simulations, *Computers and Mathematics with Applications* **78**, 437 (2019).
- [62] D. Besnard, F. H. Harlow, R. M. Rauenzahn, and C. Zemach, *Turbulence Transport Equations for Variable-Density Turbulence and Their Relationship to Two-Field Models*, Tech. Rep. LA-12303-MS, DE92 017292 (Los Alamos National Laboratory, 1992).
- [63] K. Stalsberg-Zarling and R. Gore, *The BHR2 Turbulence Model: Incompressible Isotropic Decay, Rayleigh-Taylor, Kelvin-Helmholtz and Homogenous Variable Density Turbulence*, Tech. Rep. LA-UR-11-04773 (Los Alamos National Laboratory, 2011).
- [64] F. Hamba, Analysis of Filtered Navier-Stokes Equation for Hybrid RANS/LES Simulation, *Physics of Fluids* **23** (2011).
- [65] M. Germano, Turbulence: the Filtering Approach, *Journal of Fluid Mechanics* **238**, 325 (1992).
- [66] S. Suman and S. S. Girimaji, On the Invariance of Compressible Navier-Stokes and Energy Equations Subject to Density Weighted Filtering, *Flow, Turbulence and Combustion* **85**, 383 (2010).
- [67] A. Favre, Équations Statistiques des Gaz Turbulens, *Comptes Rendus de l'Académie des Sciences Paris* **246** (1958).
- [68] A. Favre, Équations Statistiques des Gaz Turbulens Compressibles. I. Formes Générales, *Journal de Mécanique* **4**, 361 (1965).
- [69] A. Favre, Équations Statistiques des Gaz Turbulens Compressibles. II. Méthode des Vitesses Moyennes; Méthod des Vitesses Macroscopiques Pondérées par la Masse Volumique, *Journal de Mécanique* **4**, 391 (1965).
- [70] A. Favre, Équations Statistiques aux Fluctuations d'Entropie, de Concentration, de Rotationnel dans les Écoulements Compressibles, *Comptes Rendus de l'Académie des Sciences Paris* **273**, 1289 (1971).
- [71] O. Reynolds, On the Dynamical Theory of Incompressible Viscous Fluids and the Determination of the Criterion, *Philosophical Transactions of the Royal Society of*

- London **186**, 123 (1985).
- [72] J. Boussinesq, Essai sur la Théorie des Eaux Courantes, Mémoires Présentés par Divers Savants à L'Académie des Sciences **23**, 335 (1877).
- [73] J. D. Schwarzkopf, D. Livescu, J. R. Baltzer, R. Gore, and J. Ristorcelli, A Two-Length Scale Turbulence Model for Single-Phase Multi-Fluid Mixing, Flow, Turbulence and Combustion **96**, 1 (2016).
- [74] P. Tazraei and S. S. Girimaji, Scale-Resolving Simulations of Turbulence: Equilibrium Boundary Layer Analysis Leading to Near-Wall Closure Modeling, Physical Review Fluids **4**, 104607 (2019).
- [75] S. S. Girimaji and S. Wallin, Closure Modeling in Bridging Regions of Variable-Resolution (VR) Turbulence Computations, Journal of Turbulence **14**, 72 (2013).
- [76] F. S. Pereira, G. Vaz, and L. Eça, Evaluation of RANS and SRS Methods for Simulation of the Flow Around a Circular Cylinder in the Sub-Critical Regime, Ocean Engineering **186** (2019).
- [77] C. Kamble and S. Girimaji, Characterization of Coherent Structures in Turbulent Wake of a Sphere Using Partially Averaged Navier–Stokes (PANS) Simulations, Physics of Fluids **32** (2020).
- [78] F. S. Pereira, G. Vaz, L. Eça, and S. S. Girimaji, Simulation of the Flow Around a Circular Cylinder at $Re=3900$ with Partially-Averaged Navier-Stokes Equations, International Journal of Heat and Fluid Flow **69**, 234 (2018).
- [79] P. J. Roache, *Verification and Validation in Computational Science and Engineering*, 1st ed. (Hermosa Publishers, Albuquerque, United States of America, 1998).
- [80] T. G. Trucano, M. Pilch, and W. L. Oberkampf, *General Concepts for Experimental Validation of ASCII Code Applications*, Technical Report SAND2002-0341 (Sandia National Laboratories, Albuquerque, United States of America, 2002).
- [81] W. L. Oberkampf and C. J. Roy, *Verification and Validation in Scientific Computing*, 1st ed. (Cambridge University Press, Cambridge, United Kingdom, 2010).
- [82] S. S. Girimaji and K. S. Abdol-Hamid, Partially-Averaged Navier Stokes Model for Turbulence: Implementation and Validation, in *Proceedings of the 43rd American Institute of Aeronautics and Astronautics (AIAA) Aerospace Sciences Meeting and Exhibit (AIAA 2005-502*, Reno, United States of America, 2005).
- [83] S. Lakshmipathy and S. S. Girimaji, Partially Averaged Navier–Stokes (PANS) Method for Turbulence Simulations: Flow Past a Circular Cylinder, Journal of Fluids Engineering **132** (2010), 121202.
- [84] A. Elmiligui, K. S. A.-H. S. J. Massey, and S. P. Pao, Numerical Study of Flow Past a Circular Cylinder Using RANS, Hybrid RANS/LES and PANS Formulations, in *22nd Applied Aerodynamics Conference and Exhibit*, AIAA 2004-4959 (Providence, Rhode Island, USA, 2004).
- [85] B. Basara and Z. P. S. Girimaji, A New Approach for the Calculation of the Cut-Off Resolution Parameter in Bridging Methods for Turbulent Flow Simulation, International Journal of Heat and Fluid Flow **74**, 76 (2018).
- [86] L. Davidson and C. Friess, A New Formulation of f_k for the PANS model, Journal of Turbulence **20**, 322 (2019).
- [87] P. A. Davidson, *Turbulence: An Introduction for Scientists and Engineers* (Oxford University Press, 2006).
- [88] T. S. Silva, M. Zecchetto, and C. B. da Silva, The Scaling of the Turbulent/Non-Turbulent Interface at High Reynolds Numbers, Journal of Fluid Mechanics **843** (2018).
- [89] C. da Silva, *The Role of Coherent Structures in the Control and Interscale Interactions of Round, Plane and Coaxial Jets*, Phd thesis, Institut National Polytechnique de Grenoble, Grenoble, France (2001).
- [90] C. B. da Silva, S. Rego, and C. F. Pereira, Analysis of the Viscous/Molecular Subgrid-Scale Dissipation Terms in LES Based on Transport Equations: *A Priori* Tests, Journal of Turbulence **9**, N25 (2008).
- [91] C. B. da Silva and J. C. F. Pereira, Analysis of the Gradient-Diffusion Hypothesis in Large-Eddy Simulations Based on Transport Equations, Physics of Fluids **19** (2007).
- [92] V. Borue and S. A. Orszag, Local Energy Flux and Subgrid-Scale Statistics in Three-Dimensional Turbulence, Journal of Fluid Mechanics **366**, 1 (1998).
- [93] S. Liu, C. Meneveau, and J. Katz, On the Properties of Similarity Subgrid-Scale Models as Deduced from Measurements in a Turbulent Jet, Journal of Fluid Mechanics **275**, 83 (1994).
- [94] B. Vreman, B. Geurts, and H. Kuerten, Realizability Conditions for the Turbulent Stress Tensor in Large-Eddy Simulation, Journal of Fluid Mechanics **278**, 351 (1994).
- [95] U. Schumann, Subgrid Scale Model for Finite Difference Simulations of Turbulent Flows in Plane Channels and Annuli, Journal of Computational Physics **18**, 376 (1975).
- [96] R. S. Rogallo and P. Moin, Numerical Simulation of Turbulent Flows, Annual Reviews of Fluids Mechanics **16**, 99 (1984).
- [97] M. Gittings, R. Weaver, M. Clover, T. Betlach, N. Byrne, R. Coker, E. Dendy, R. Hueckstaedt, K. New, W. R. Oakes, D. Ranta, and R. Stefan, The RAGE Radiation-Hydrodynamic Code, Computational Science & Discovery **1** (2008).
- [98] E. F. Toro, M. Spruce, and W. Speares, Restoration of the Contact Surface in the HLL-Riemann Solver, Shock Waves **4**, 25 (1994).
- [99] P. Colella and P. R. Woodward, The Piecewise Parabolic Method (PPM) for Gas-Dynamical Simulations, Journal of Computational Physics **54**, 174 (1984).
- [100] B. Thornber, A. Mosedale, D. Drikakis, D. Youngs, and R. J. R. Williams, An Improved Reconstruction Method for Compressible Flows with Low Mach Number Features, Journal of Computational Physics **227**, 4873 (2008).
- [101] B. van Leer, Towards the Ultimate Conservative Difference Scheme, Journal of Computational Physics **135**, 229 (1997).
- [102] J. Jeong and F. Hussain, On the Identification of a Vortex, Journal of Fluid Mechanics **285**, 69 (1995).
- [103] J. C. R. Hunt, A. A. Wray, and P. Moin, *Eddies, Stream, and Convergence Zones in Turbulent Flows*, techreport CTR-S88 (Center for Turbulence Research, Stanford University, Stanford, California, United States of America, 1988).
- [104] F. S. Pereira, L. Eça, G. Vaz, and S. S. Girimaji, Toward Predictive RANS and SRS Computations of Turbulent External Flows of Practical Interest, (submitted) (2020).
- [105] A. K. M. F. Hussain and W. C. Reynolds, The Mechanics of an Organized Wave in Turbulent Shear Flow, Journal of Fluid Mechanics **41**, 241 (1970).

- [106] R. Schiestel, Multiple-Time-Scale Modeling of Turbulent Flows in One-Point Closures, *Physics of Fluids* **30**, 722 (1987).
- [107] L. Eça and M. Hoekstra, A Procedure for the Estimation of the Numerical Uncertainty of CFD Calculations Based on Grid Refinement Studies, *Journal of Computational Physics* **262**, 104 (2014).
- [108] F. S. Pereira, F. F. Grinstein, D. M. Israel, and R. Rauenzahn, Molecular Viscosity and Diffusivity Effects in Transitional and Shock-Driven Mixing Flows, (submitted) (2020).
- [109] D. Virk, F. Hussain, and R. M. Kerr, Compressible Vortex Reconnection, *Journal of Fluid Mechanics* **304**, 47 (1995).
- [110] F. S. Pereira, *Towards Predictive Scale-Resolving Simulations of Turbulent External Flows*, Ph.D. thesis (2018).
- [111] F. S. Pereira, L. Eça, G. Vaz, and M. Kerkvliet, Application of Second-Moment Closure to Statistically Steady Flows of Practical Interest, *Ocean Engineering* **189** (2019).